E2E Physical Layer and Link Analysis for High-Throughput Satellite Optical Communication

Veronica Spirito, Ernesto Ciaramella, *Senior Member, IEEE*, and Giulio Cossu, *Member, IEEE*

***Abstract*—Satellite optical communications will revolutionize global high-speed connectivity. In this paper, we carry out a comprehensive evaluation of end-to-end (E2E) Wavelength Division Multiplexing (WDM)-Free Space Optical Communication (FSOC) systems to establish high-performance Earth-GEO links using a semi-analytical tool. We present a novel method to accurately compute the divergence of a truncated and obscured beam, typical of Cassegrain telescopes; this model is instrumental to optimize the beam divergence with Pointing Error (PE) and beam wander. The effects of beam wander, scintillation, and PE are first individually investigated to derive the required margins for different outage probabilities (OPs), followed by an assessment of Adaptive Optics (AO) benefits and limitations. Furthermore, we comprehensively assess the uplink and downlink systems, exploiting for the first time an innovative and fully analytical closed-form expression to describe the combined three statistical effects. Finally, the full system analysis is carried out in the challenging scenario of strong turbulence, at various elevation angles and OP targets. By considering both coherent and non-coherent systems adopted from fiber communications, we determine the transmitter power and the maximum achievable throughput.**

***Index Terms*—Free space optical communications, non-terrestrial networks, optical feeder link, optical terminals, optical wireless communication, satellite optical communications, space laser communications, very high throughput satellites, wavelength division multiplexing.**

I. Introduction

FIBER Optical Communications (FOCs) revolutionized terrestrial networks, and now Free Space Optical Communications (FSOCs) are entering the domain of satellite communications. High-speed satellite links are urgently needed for various applications, such as Earth observation, disaster recovery, and last mile access of white areas. Whilst the Radio Frequency (RF) communications approach their limits, the adoption of FSOC is imperative for satellite operators, seeking a substantial increase of capacity [1].

A future satellite optical network, as depicted in Fig. 1, uses various optical link types, including Feeder-links (FLs) (ground-space uplink and downlink), Inter-Satellite link (ISL), and potentially deep-space links [2]. This evolution is facilitated by adopting the license-free C-band (1530 – 1565 nm), with its low attenuation in both fibers and atmosphere. At the same time, it allows for interoperability with the terrestrial network, leveraging a well-established legacy and technology that can be largely re-adapted for satellite communications. A key advantage lies in the Wavelength Division Multiplexing (WDM) technology, allowing for a substantial increase in overall capacity (e.g., up to 1 Tbit/s). In addition, Erbium-Doped Fiber Amplifiers (EDFAs), developed for FOC, are crucial for transmitting high-throughput over long distances. However, adopting FOC commercial transceivers limits the specific choices, e.g., in terms of bit-rate, modulation formats, Digital Signal Processing (DSP) implementation [3].

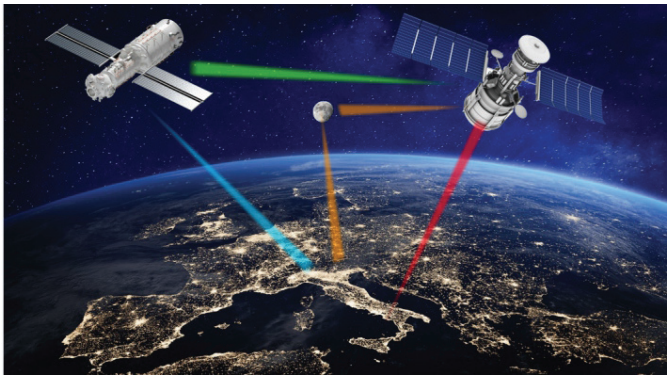

Fig. 1. Pictorial view of FSO links in a satellite communication network: two FLs (uplink in red, downlink in light blue), one ISL (in green) and one deep-space links (in orange).

Different initiatives are underway to develop high-speed FSOC systems, with in-orbit demonstrations of laser-based technology taking place worldwide. Today, space agencies and private companies are heavily investing in programs and missions to establish optical ISLs and FLs, passing through the atmosphere. As remarkable examples, TeraByte InfraRed Delivery (TBIRD) by National Aeronautics and Space Administration (NASA) is demonstrating 200 Gbit/s CubeSat-based optical terminals [4]; Space-X Starlink [5] and Amazon Kuiper [6] are demonstrating 100 Gbit/s Low-Earth-Orbit (LEO) ISLs. The Japan Aerospace Exploration Agency (JAXA) Japanese Data Relay System (JDRS) program for Earth observation is adopting an inter-orbit optical link [7].

Indeed, most of the actual realizations focus on ISLs, as FLs pose key challenges related to the time-variant

Received 5 April 2024; revised 14 September 2024; accepted 7 November 2024. Date of publication 5 March 2025; date of current version 14 May 2025. This work was supported in part by the European Union—Next Generation EU under the Italian National Recovery and Resilience Plan (NRRP), Mission 4, Component 2, Investment 1.3, CUP J53C22003120001, Partnership on "Telecommunications of the Future" (PE00000001—Program "RESTART"). *(Corresponding author: Veronica Spirito.)*

Veronica Spirito was with the Sant'Anna School of Advanced Studies, TeCIP, 56127 Pisa, Italy. She is now with European Space Research and Technology Centre, European Space Agency, 2201 AZ Noordwijk, The Netherlands (e-mail: veronica.spirito@ext.esa.int).

Ernesto Ciaramella and Giulio Cossu are with the Sant'Anna School of Advanced Studies, TeCIP, 56127 Pisa, Italy.

Digital Object Identifier 10.1109/JSAC.2025.3545985

atmosphere, which results into random attenuation, deviation, and degradation of the light-wave signal [8]. A notable example is the French TELEO demonstration, hosted on a commercial satellite launched in May 2023, which aims to collect crucial information on the channel effects and mitigate risks associated with the key technologies of the on-board terminal [9]. A parallel activity is the development of French Optical Ground Station (FrOGS), which will be used for a LEO-to-ground demonstration and to test some building blocks for optical feeder during TELEO demo [10]. Successful high-throughput communications have also been demonstrated by DLR [11], [12], including earlier efforts [13], [14].

Among FLs, designing Earth to/from Geostationary-Earth-Orbit (GEO) links is the most challenging task, because propagation effects combine with the longest distance, and many impairments should be considered, which can all affect the quality of the received signal. GEO satellites, positioned at a high altitude, can provide broad coverage. Thus, they are the ideal candidates for several applications and deep space relay nodes [15]. Promising GEO-to-ground flight demonstrations and new Optical Ground Station (OGS) developments are progressing worldwide. A joint research initiative between JAXA and National Institute of Information and Communications Technology (NICT) realized an experimental analysis of the atmospheric channel model under different turbulence conditions for GEO satellite-to-ground optical links, using the Laser Utilizing Communication Systems (LUCAS) system onboard an optical data relay GEO satellite [16]. Numerous R&D activities are in place also in the framework of European Space Agency (ESA) High thRoughput Optical Network (HydRON) program, which aims at developing a "fiber in the sky" network [1], while Australian Space Agency (ASA) is investigating solutions to further mitigate the atmospheric effects [17].

Although several groups are investigating these topics, in the present scientific literature, the many different atmospheric effects were described separately and, in many cases, partially. We thus developed an holistic approach to Earth-GEO FSOC link design, with enhanced modeling accuracy. To this aim, we refined the models of various physical effects and included them in the system design. As an example, the effect of beam truncation and obscuration due to the transmitter telescope was investigated in [18] and [19], but no closed-form equation was given for the resulting divergence due to the combined effects. In this work, we devise a novel method to accurately calculate the divergence angle of a truncated and obscured beam, essential for determining the optimal Transmitter (TX) telescope diameters and mitigating the impacts of Pointing Error (PE) and beam wander. Initially, beam wander, scintillation and PE are investigated individually, reporting the losses required to account for different outage probability (OP) values and determining the benefits introduced by the Adaptive Optics (AO) [20], [21], [22]. The combined statistics of the three effects is examined and discussed: we exploit a novel and fully analytical closed-form expression for accurately computing the link budgets, which models effectively the three stochastic phenomena and was recently derived [23]; in this work, we use it for the first time in a system design.

We then apply our holistic approach to determine new design criteria. Remarkably, we calculate, for the first time to our knowledge, the general interplay between the signal divergence and the PE or the beam wander in uplink. In previous studies, this was only considered after a successful pre-distortion was applied [24], [25], [26], [27]; in contrast, our new formulation is broadly applicable, and it is also valid to compute the optimal divergence in the conditions of no beam-wander pre-distortion, which is typical of the onset of the communication.

We also numerically derive the optimized diameter of the OGS and the GEO telescopes. This type of analysis has few precedents: among them, the most similar trade-off study was presented in [24]. From that reference, we observe several significant differences in our approach: the antenna gain accounts for beam truncation and obscuration, which in turn increases the divergence; the beam wander effect is assessed by considering the correlation between downlink and uplink signals; the pointing loss, which is significantly influenced by the transmitter diameter, is explicitly included into the trade-off. Finally, in both downlink and uplink, we quantify the communication benefits of implementing AO technique in mitigating the impairments associated with atmospheric effects. In particular, we also assess the limitations due to the anisoplanatism and the residual phase distortions.

We can thus present the results of a comprehensive model, obtained by using a numerical tool written in MATLAB®. By means of a semi-analytical approach, the tool evaluates an end-to-end (E2E) point-to-point WDM-FSOC link to/from Earth GEO satellites. We investigate three different modulation formats, highlighting the advantages and the disadvantages when using them in a system working through a turbulent atmosphere. We determine the required optical TX power to enable the link for a specific target OP. Therefore, for different system parameters, we determine the maximum achievable aggregate throughput while keeping the transmitted power and system complexity within practical constraints. The methodology and the obtained results can represent a useful guideline for future design of these FSOC systems.

The paper is organized as follows. In Section II, we outline the models used to assess the feasibility of the Earth-GEO satellite links. We provide a detailed analysis and a numerical validation of the realistic assumptions made in this study. Furthermore, we describe a novel composite probability density function (pdf) for the fading channel, which combines the statistical impairments. In Section III, we numerically explore the mitigation techniques, reporting the advantages and constraints. Following that, in Section IV, we use these models to conduct a trade-off analysis determining the optimal diameters of the OGS/GEO telescopes, aiming to maximize the Receiver (RX) optical power. In Section V, we discuss the benefits and drawbacks of three modulation schemes (On-Off-Keying (OOK), Differential Phase Shift Keying (DPSK) and Dual Polarization Quadrature Phase-Shift Keying (DP-QPSK)), commonly considered in FSOC. Section VI presents the link budget analyses and the communication results for both uplink and downlink. Finally, in Section VII, we draw the conclusion and suggest future research needs.

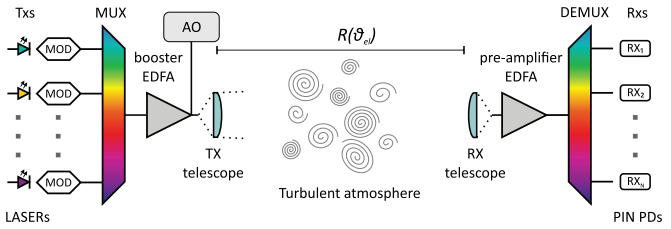

Fig. 2. Typical transparent WDM-FSO system for the uplink. WDM channels are modulated (MOD), combined (MUX), amplified (EDFA), and pre-corrected by an adaptive optics (AO) system before transmission. At the receiver (RX), the signal is collected, amplified, demultiplexed (DEMUX), and detected. MOD: Modulator, MUX: Multiplexer, EDFA: Erbium-Doped Fiber Amplifier, AO: Adaptive Optics, DEMUX: De-Multiplexer.

II. Simulation Model

We consider a realistic scenario where the OGS is located in Tenerife at 2393 m above sea level, and the GEO satellite at an altitude of 35 789 km. Tenerife was chosen to leverage the existing OGS established by ESA, equipped with 1 m telescope. Clear sky is assumed, meaning the absence of significant cloud cover, though still subject to natural atmospheric turbulence. Under clear sky, the system is expected to work in most of the conditions. The presence of clouds would require site-diversity techniques, warranting a dedicated study. Moreover, since the turbulence changes during the day, we design the system according to the worst case condition, i.e., strong turbulence, as defined in Section II-F.

A. WDM Optical System

The space industry is moving to a second generation of FSOC system that exploits WDM technology to increase the overall network capacity. This advancement is boosted by new terminals that interface free-space with optical fibers seamlessly, both at the TX and RX ends [3], [28].

A conceptual representation of a transparent WDM-Free Space Optics (FSO) for the uplink is depicted in Fig. 2. At the ground-based TX, the WDM channels are combined by a Multiplexer (MUX), amplified by a booster EDFA, and launched from the TX telescope. Before reaching the satellite, the signal travels through the atmosphere, experiencing various impairments that are (partly) pre-corrected by the AO system. The lightwave is collected by RX telescope on-board, and amplified by means of a space-qualified EDFA pre-amplifier. Eventually, the channels are demultiplexed and filtered by a De-Multiplexer (DEMUX), and detected by conventional RXs, each performing signal photodetection, clock and data recovery, and decoding.

In downlink, the on-board TX, similar to the ground-based one, transmits the WDM signal to the OGS. Here, the AO system plays a key role in improving the efficiency of coupling the light into a single-mode fiber (SMF). At the fiber output, the optical signal is amplified by a low-noise EDFA, demultiplexed. Finally, the information is extracted by means of the ground-based RX. We note that in WDM systems the crosstalk effects among the channels are negligible thanks of the use of commercial WDM demultiplexers for fiber optics. These devices have an excellent performance, with cross-talk levels lower than −50 dB, between neighboring channels [29].

On satellites, the implementation of the AO is not helpful, being in the far-field region, and surely it is not feasible due to various technical and operational constraints. These include mass and volume limitations, power consumption, vibrations and mechanical stability, and challenges associated with pointing and tracking. Consequently, the alternative strategy encompasses ground-based AO systems that pre-compensate for the channel impairments in the uplink transmission.

B. Link Budget Contributions

In order to assess the performance of such FSO systems, a link budget analysis is conducted to estimate the received power P_R given the transmitted power P_T. This is done by considering the number of WDM channels N_{ch}, the system and channel contributions:

$$P_R = \frac{P_T}{N_{ch}} G_T \eta_T G_R \eta_R L_{FSO} L_{atm} L_{fc} M_{pdf} \tag{1}$$

In this equation, G_T (η_T) and G_R (η_R) are the antenna gains (efficiencies) of TX and RX telescopes, respectively. L_{FSO} refers to the geometrical FSO loss, L_{atm} denotes the deterministic atmospheric losses assuming clear sky conditions. Additionally, L_{fc} is the fiber coupling loss, and M_{pdf} is the maximum loss accounting for statistical effects of pointing, scintillation and beam wander, which are combined in a single composite pdf. However, to assess and mitigate the impact of each impairment, we also compute separate losses for the three statistical contributions: pointing error, beam wander, and scintillation effects. This approach isolates the individual statistical contributions by using independent pdfs $f(I)$ for each effect. The resulting maximum loss denoted M_p, M_{bw}, and M_s, respectively, provide targeted adjustments for each specific effect. These are derived by evaluating the corresponding cumulative distribution function (cdf) $F(x)$, which is equivalent to the OP. We consequently determine the value such that the confidence interval is equal to the targeted OP, by inverting the equation [30]:

$$M_{\{p,bw,s\}} = F^{-1}_{\{p,bw,s\}}(\text{OP}) \tag{2}$$

We consider 4 dB margin accounting for minor effects, including uncertainties in component performance, aging, and thin clouds.

We also highlight that MUX and DEMUX do not contribute to the link budget: since the booster amplifier operates in saturation, the insertion loss of the MUX is neglected. On the other side, as the pre-amplifier provides sufficient gain at RX (around 30 dB), the output power of each channel will largely exceed the power-sensitivity of the transceiver, even when taking into account the (low) insertion loss of the DEMUX (typically 5 dB).

C. Gaussian Beam Through a Telescope

In the context of the seamless interface between free-space and SMF optical fibers described in Section II-A, a Gaussian beam is launched through a telescope, acting as an

optical antenna. However, due to its finite aperture, the beam undergoes truncation. Moreover, the presence of a central secondary mirror – common in Cassegrain telescopes – further affects the propagation [31] by not only truncating the beam, but also introducing obscuration. The combined effects not only reduce the TX/RX on-axis gain, but also increase the divergence angle of the optical beam [18], [19], which impacts on the pointing error and the beam wander effect, as we elaborate further.

The divergence angle in the far-field for a diffraction-limited Gaussian beam is [32]:

$$\theta_d = \frac{2\lambda}{\pi D_T} \tag{3}$$

where λ is the central wavelength and D_T is the diameter of the TX telescope. However, this expression does not account the finite telescope aperture or the obscuration. Several works discussed the far-field patterns of truncated Gaussian beam [18], [19], [33], [34]. Among them, [18] provides the detailed analysis of far-field profile of the truncated and obscured Gaussian beam $g_T(\gamma_t, \theta)$ as a function of the off-axis angle θ [18]. This profile term is referred as *transmitter efficiency factor* and it is determined by [18, Eq. (7)]:

$$g_T(\gamma_t, \theta) = 2\alpha_t^2 \left| \int_{\gamma_t^2}^{1} \exp\left(-\alpha_t^2 v\right) J_0\left(k \frac{D_T}{2} \theta \sqrt{v}\right) dv \right|^2 \tag{4}$$

In this equation, $k = 2\pi/\lambda$, α_t is the truncation factor, which is defined as the ratio between the aperture radius of the telescope, $D_T/2$, and the beam waist, W_0. γ_t indicates the obscuration factor, defined as the ratio between the aperture and obscuration radius, J_0 denotes the zero-order Bessel function of the first kind, and v is defined as $(2r/D_t)^2$, where r is the telescope radius integration variable. The solution of Eq. (4) allows to determine the on-axis antenna gain factor (hence, the transmitted power from the telescope) and the beam divergence, crucial parameters when designing a FSO link. The truncated and obscured on-axis gain is then derived by combining the well-known formula of the telescope gain [35, Eq. (3)] and Eq. (4), computed for $\theta = 0$ rad. This yields:

$$\begin{aligned} G_T &= \left(\frac{\pi D_T}{\lambda}\right)^2 g_T(\gamma_t, 0) \\ &= \left(\frac{\pi D_T}{\lambda}\right)^2 \frac{2}{\alpha_t^2} \left(e^{-\alpha_t^2} - e^{-\alpha_t^2 \gamma_t^2}\right)^2. \end{aligned} \tag{5}$$

The gain G_T is maximized when $\alpha_t \approx 1.12 - 1.30\gamma_t^2 + 2.12\gamma_t^4$ for a given obscuration factor γ_t [18, Eq. (12)]. For instance, if we consider a telescope with only truncation effects ($\gamma_t = 0$), for the optimal α_t (1.12), we obtain around 1 dB reduction of total power, compared to the ideal Gaussian beam. On the other side, if we have a 30% obscuration and the optimized truncation, the on-axis gain decreases by 2 dB from the unobscured and non-truncated Gaussian beam.

To determine the beam divergence of a truncated and obscured optical beam, we numerically solve Eq. (4), varying γ_t and optimizing α_t. The resulting curves, for typical γ_t values, are depicted in Fig. 3, as a function of the off-axis angle θ normalized to θ_d (as in Eq. (3)). For the sake of clarity, the off-axis beam profile $g_T(\gamma_t, \theta)$ is reported normalized to the on-axis value $g_T(\gamma_t, 0)$. The angle at which the power reduces by a factor $1/e^2$ represents the divergence angle $\hat{\theta}_d$ of the truncated and obscured beam. As expected, even in absence of obscuration, the divergence angles exceed θ_d values ($\theta/\theta_d > 1$), i.e., the truncated (and obscured) beam diverges more than the diffraction-limited Gaussian beam. As an example, $\hat{\theta}_d = 1.23\,\theta_d$, considering $\gamma_t = 0.4$ ($\alpha_t \simeq 0.98$ for the optimized G_T).

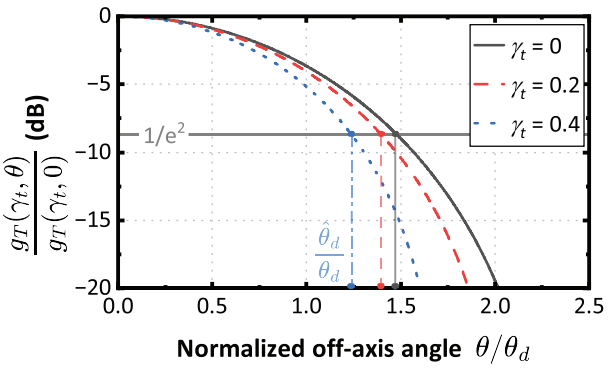

Fig. 3. Beam profile versus the off-axis angle θ normalized to the diffraction limited divergence angle θ_d, for $\gamma_t = \{0, 0.2, 0.4\}$ and, in each case, α_t was optimized as explained in the text. The beam power is normalized to the on-axis value $g_T(\gamma_t, 0)$. We define the normalized divergence angles ($\hat{\theta}_d/\theta_d$) as the ratio θ_d/θ_d where the power reduces by $1/e^2$ (see the vertical lines). These curves, obtained by using Eq. (4), highlight the increased divergence of truncated and obscured beams compared to the ideal diffraction-limited Gaussian beam.

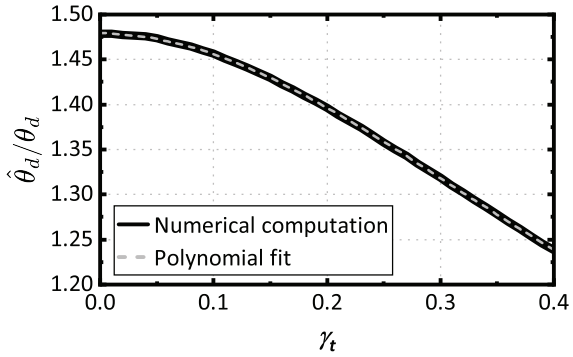

Fig. 4. Divergence angle $\hat{\theta}_d$ of a truncated and obscured beam, normalized to θ_d (divergence of the ideal Gaussian beam) as a function of the obscuration factor γ_t (again, α_t was optimized as explained in the text). The solid line indicates the numerical computation of the normalized divergence angle from Fig. 3, while the dashed gray curve shows the polynomial fit (reported in Eq. (6)).

We then also perform numerical calculations for the parameter $\hat{\theta}_d$ at different γ_t values. This parameter can be expressed as a function of θ_d and a coefficient that depends only on γ_t, i.e., $\hat{\theta}_d = f(\gamma_t)\theta_d$. To determine this coefficient, in Fig. 4, we present $\hat{\theta}_d/\theta_d$ as a function of γ_t, ranging from 0 to 40%. We found that this curve can be well approximated with a 3rd order polynomial equation:

$$f(\gamma_t) \approx 1.48 - 2.64\gamma_t^2 + 2.84\gamma_t^3 \tag{6}$$

This is a compact and useful form, which can be used in further studies of similar systems. For instance, the beam divergence increases by a factor 1.48 solely due to the

truncation factor (without any obscuration), with optimized α_t. The coefficient decreases at larger obscuration factor. This approximation greatly simplifies the estimation of the beam divergence by applying a coefficient to Eq. (3), with the parameter γ_t (and considering the optimal truncation factor that maximize the on-axis gain of Eq. (5)).

A similar approach was used to determine the RX antenna gain, with obscuration γ_r [36]. The on-axis RX gain is given by:

$$G_R = \left(\frac{\pi D_R}{\lambda}\right)^2 \left(1 - \gamma_r^2\right) \tag{7}$$

where D_R represents the diameter. Finally, in this work, both telescopes are assumed to have the same efficiency, i.e., $\eta_T = \eta_R = 50\%$.

D. Free Space Loss

The free-space loss increases with the square of distance. This is a crucial aspect in long-range communications, since it causes the majority of the losses. We express it by:

$$L_{FSO} = \left(\frac{\lambda}{4\pi R(\vartheta_{el})}\right)^2 \tag{8}$$

where $R(\vartheta_{el})$ is the line-of-sight between the OGS and the satellite, which depends on the elevation angle ϑ_{el}. This length is known as slant range and is given by [37]:

$$R(\vartheta_{el}) = \sqrt{H^2 + 2HR_E + R_E^2 \sin(\vartheta_{el})^2} - R_E \sin(\vartheta_{el}) \tag{9}$$

where H is the satellite altitude from the ground, R_E the Earth radius. In addition, the actual propagation path may vary depending also on the height of the OGS. Typical free-space losses for an Earth to GEO link (35 789 km) are around 290 dB.

E. Residual Pointing Error

Satellite-borne optical communication systems require a very accurate alignment (< 10 μrad) between TX and RX, which must be consistently maintained throughout the communication. This task is carried out by the Pointing, Acquisition and Tracking (PAT) subsystem. Once a well-aligned line-of-sight is provided between the terminals, the link is established. Yet, communication performance can still be influenced by residual PE. The PE originates from two main sources: random tracking errors and systematic point-ahead errors [2]. Combined, these errors typically result in a PE between 1 and 5 μrad. Compared to typical beam divergences of a few μrad, the residual pointing error can pose significant challenges for reliable space-based FSO systems.

The PE θ_p is commonly described by a Gaussian distribution for both independent axes, with standard deviation $\sigma_{\theta,p}$ and mean $\mu_{\theta,p}$ [27]. In absence of the bias error $\mu_{\theta,p}$, the pdf of the PE follows the well-known Rayleigh distribution [27]:

$$p_j(\theta, \sigma_{\theta,p}, 0) = \frac{\theta}{\sigma_{\theta,p}^2} \exp\left(-\frac{\theta^2}{2\sigma_{\theta,p}^2}\right) \tag{10}$$

where θ is the angular offset from the optical axis.

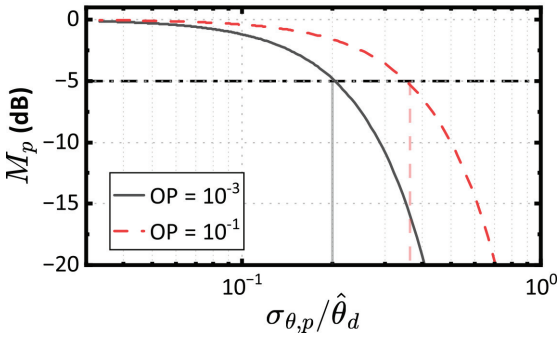

Fig. 5. M_p as a function of the pointing jitter $\sigma_{\theta,p}$ normalized to the optimal beam divergence angle $\hat{\theta}_d$, for two OP values: 1×10^{-3} and 1×10^{-1}. These curves were derived from Eq. (12) and indicate the ratio between the pointing jitter and divergence angle to obtain a M_p for a specific OP. These insights emphasize the trade-off between beam divergence and residual pointing jitter for robust space-based FSO communication links.

Since the far-field irradiance of a Gaussian beam I is proportional to $\exp\left(-2\theta^2/\hat{\theta}_d^2\right)$, the corresponding intensity distribution $f(I)$ follows the beta distribution:

$$f(I) = qI^{q-1} \text{with } 0 \le I \le 1 \tag{11}$$

where $q = (\hat{\theta}_d/2\sigma_{\theta,p})^2$. As can be noted, the intensity distribution due to pointing depends on the ratio between the divergence angle $\hat{\theta}_d$ and the pointing jitter $\sigma_{\theta,p}$.

To evaluate M_p, we applied the method described in Section II-B, specifically using Eq. (2), which gives:

$$M_p = 10 \log_{10}\left(\text{OP}^{\frac{1}{q}}\right) \tag{12}$$

In Fig. 5, we report M_p as a function of the pointing jitter $\sigma_{\theta,p}$, conveniently normalized with the divergence angle $\hat{\theta}_d$, for two target OPs. It is worth noting that when the beam divergence and the residual pointing jitter are equal ($\sigma_{\theta,p}/\hat{\theta}_d = 1$), a significant high margin ($\gg$ 20 dB) must be considered in the link budget to meet the target OP. To achieve an acceptable pointing margin ($|M_p| < 5$ dB), a divergence at least 2.7× wider than the pointing jitter is required ($\hat{\theta}_d \approx 2.7\sigma_{\theta,p}$), considering a target OP of 1×10^{-1} (5× for OP = 1×10^{-3}).

F. Atmospheric Channel and Related Beam Impairments

In addition to the free-space losses, the main challenge in a FL arises from the interaction of the light with the time-variant channel. Along the propagation path, the beam experiences different atmospheric effects due to particles of different sizes and shapes, as well as random local refraction index fluctuations – referred as turbulent eddies – resulting in fading and beam degradation. Comparing the size of the turbulent eddies and the optical beam waist reveals an asymmetric degradation between uplink and downlink. In uplink, the beam suffers the atmospheric effects as soon as it leaves the OGS and becomes strongly distorted while spreading. This mostly leads to scintillation, beam spreading and beam wander. Conversely, in downlink, the turbulent channel occurs at the end of the propagation path, after the optical beam has already experienced spreading due to diffraction. This results

mainly in phase distortions. The more atmosphere the light passes through, the greater the accumulated effects, resulting in stronger distortions observed at lower elevation angles, where the slant range is longer.

During the last decades, various mathematical approaches were developed to model the atmospheric effects, aiming to implement effective countermeasures and improve the link performance. We shortly summarize the deterministic attenuation, followed by a description of the probabilistic atmospheric beam effects.

1) Deterministic Impairments: Deterministic attenuation is caused by suspended molecules and aerosols that absorb and scatter the incident photons. The absorption attenuation follows the well-known exponential Beer's-Lambert equation, characterized by the wavelength-dependent atmospheric transmittance parameter $T(\lambda)$ [38]. Various transmission modeling software – now considered reliable and accurate – were developed to calculate the transmittance and the corresponding absorption coefficient. Among them, we mention MODTRAN®, which we used to estimate the atmospheric transmittance. In our analysis, assuming a clear sky scenario, we found that the atmosphere is nearly transparent in the optical C-band, with an average $T(\lambda) = 0.93$ at zenith, resulting in an absorption penalty < 1 dB.

In the same optical window, Mie scattering is dominant since the size of the scattering element is comparable to the wavelength of the light. This introduces a loss coefficient α_{scatt} given by [39]

$$\alpha_{\text{scatt}}(V,\lambda) = \frac{17}{V}\left(\frac{\lambda}{550}\right)^{-q(V)}, \tag{13}$$

where α_{scatt} is given in dB/km, V is the meteorological visibility expressed in km [40], λ is the wavelength expressed in nanometers, and $q(V)$ represents the particle size distribution [38], [39]. We estimate the total atmospheric loss – expressed in dB – as:

$$L_{atm} = [T(\lambda)\sec(\vartheta_{el})]_{dB} + \alpha_{scatt}(V,\lambda)R(\vartheta_{el}) \tag{14}$$

In our scenario, the atmospheric attenuation ranges from 0.8 to 2.5 dB, as the elevation angle decreases from zenith to 30°.

2) Scintillation and Beam Wander: the most challenging estimation concerns the random variations of refractive indices, which create turbulent air eddies, with varying densities and sizes. When smaller than the beam waist, these eddies act like prisms and lenses, producing constructive and destructive interference effects on the wavefront. This results in a signal with an intensity that randomly changes over time and space, known as *scintillation*. The temporal correlation of these fluctuations is expressed by means of the atmospheric coherence time [41, Eq. (98),p. 637], and typically is in the range of 1 ms to 100 ms.

The most generally accepted and non-site-specific model to describe the fluctuation strength along the vertical propagation path is the Hufnagel-Valley (HV) model [41], which was later modified to consider an OGS not located at sea level. It is characterized by the refractive index structure parameter $C_n^2(h)$, which is given by:

$$C_n(h)^2 = 5.95\times10^{-53}\left(\frac{w}{27}\right)^2 h^{10}e^{\frac{-h}{1000}} + 2.7\cdot10^{-16}e^{\frac{-h}{1500}} + Ae^{\frac{-(h-h_0)}{100}}e^{\frac{-h_0}{700}} \tag{15}$$

In this equation, A depends on the OGS altitude h_0, temperature, pressure, and the structure parameter value of $C_n^2(0)$ at the sea level. h is the altitude, while w denotes the root mean square (rms) wind speed at high altitude, as detailed in [41], taking into account the most accurate and validated Bufton wind profile [42]. The turbulence near the ground up to around the first km is largely dependent on $C_n^2(0)$ and higher is the OGS altitude, less the turbulence-induced beam effects. However, from approximately 2.5 km the influence of wind speed w becomes significant, as it can be observed in Fig. 6. The higher is the OGS altitude, the lower the turbulence-induced beam effects, especially in the first kilometers.

Due to the scintillation, the irradiance at the RX pupil plane varies randomly, depending on the turbulence strength. Specific conditions are identified by the Fried parameter r_0, also known as coherence diameter, which is the length over which the wavefront typically exhibits a phase variation lower than 1 rad [43, Eq. 3.51]. r_0 increases as the turbulence decreases,

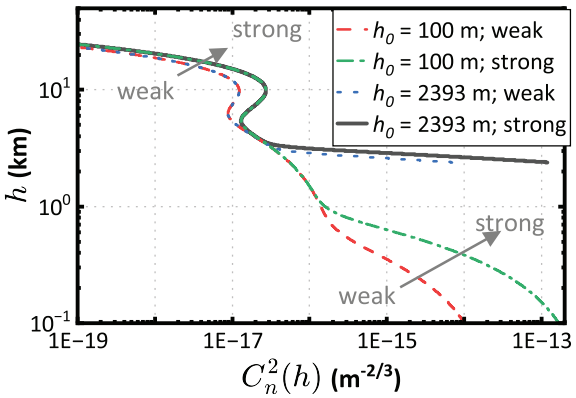

Fig. 6. $C_n^2(h)$ curves considering different strength at ground, wind speed and OGS altitude values. It strongly depends on $C_n^2(0)$ and OGS altitude up to the first kilometers; above that, the wind speed has an impact. The curves were generated from Eq. (15), for different input parameters, i.e., two OGS altitudes: $h_0 = \{100\text{ m}, 2393\text{ m}\}$ and two atmospheric conditions: *weak* $C_n^2(0) = 10^{-14}\text{m}^{-2/3}$, $w = 18$ m/s and *strong* $C_n^2(0) = 1.7\times10^{-13}\text{m}^{-2/3}$, $w = 27$ m/s.

TABLE I
SUMMARY OF THE SCENARIO PARAMETERS AND RELEVANT COMPUTED ATMOSPHERIC OUTPUTS

Parameter	Value	Condition
GEO Satellite altitude	35 789 km	at zenith
OGS altitude	2393 m	Tenerife site
C_n^2 at ground	1.7×10^{-13} m$^{-2/3}$	
Wind speed	27 m/s	
Visibility	15 km	
Atmospheric transmittance	0.93	clear sky, at zenith, C-band
Greenwood frequency	85 – 130 Hz	$\vartheta_{el} = 30-90°$
Fried parameter @ 1550 nm	4.5 – 7 cm	$\vartheta_{el} = 30-90°$
σ_I^2	0.1 – 0.4	$\vartheta_{el} = 30-90°$
D_R/r_0	3×10^{-4} – 4×10^{-4}	$\vartheta_{el} = 30-90°$, uplink
D_R/r_0	14 – 25	$\vartheta_{el} = 30-90°$, downlink

typically ranging from a few centimeters to tens of centimeters in strong and weak turbulence conditions, respectively. In our analyses, we considered a challenging scenario characterized by strong turbulence with $C_n^2(0) = 1.7 \times 10^{-13}\text{m}^{-2/3}$ and $w = 27$ m/s. In this scenario, W_0/r_0 varies approximately between 1.4 – 2.2, as the elevation decreases from the zenith to 30°. The relevant scenario parameters considered in this study are summarized in Table I.

Various statistical models were developed to characterize the random fluctuations of the instantaneous intensity. Among these, it was verified that the log-normal distribution effectively characterizes weak intensity fluctuations [16], [44], [45]. However, the widely accepted Gamma-Gamma ($\mathcal{GG}$) distribution provides a reasonably accurate model under a wide range of turbulence conditions, encompassing both weak and strong turbulence scenarios and experimentally confirmed [16], [44], [45]. Indeed, in the weak turbulence condition, $\mathcal{GG}$ distribution converges to the log-normal distribution. Furthermore, our calculations and findings in other studies [45] indicate that in the weak turbulence regime, the log-normal distribution can be replaced by the Gamma ($\mathcal{G}$) distribution when the elevation angle ϑ_{el} exceeds 30°. All these pdfs are characterized by the variance normalized by the mean irradiance of the fluctuation, generally referred as Scintillation Index (SI): $\sigma_I^2 = \left(\langle I^2\rangle - \langle I\rangle^2\right)/\langle I\rangle^2$.

In this work, we used Gamma-Gamma $\mathcal{GG}$ to describe the uplink scintillation distribution, which is thus mathematically given by:

$$f_I(I) = \frac{2(ab)^{\frac{a+b}{2}}}{\Gamma(a)\Gamma(b)I}\left(\frac{I}{\langle I\rangle}\right)^{\frac{a+b}{2}} K_{a-b}\left(2\sqrt{\frac{abI}{\langle I\rangle}}\right) \tag{16}$$

where I is the intensity at the RX, Γ and K are respectively the Gamma function and modified Bessel function of the second kind. The variables a and b (small and large scale turbulent cells, respectively) are defined as in [41].

However, Eq. (16) could give computational issues when the SI is small (i.e., when a and b are large). Therefore, in downlink, where the SI benefits from aperture averaging (see Section III), we opt for $\mathcal{G}$ distribution, which is defined as

$$f_I(I) = \frac{1}{\Gamma(m)I}\left(\frac{mI}{\langle I\rangle}\right)^m e^{-\frac{mI}{\langle I\rangle}} \tag{17}$$

where $m = \left(\exp\left(\sigma_{\ln X}^2 + \sigma_{\ln Y}^2\right) - 1\right)^{-1}$, with $\sigma_{\ln X}^2$ and $\sigma_{\ln Y}^2$ denoting the small-scale and large-scale log-irradiance variance values, as reported in [45].

Other turbulence-induced phenomena, including beam spreading beyond geometric diffraction limits, speckle effects, and beam wander, contribute to the complexity of channel impairments estimation. In particular, beam wander results in an apparent angular displacement of the optical beam around its bore-sight position at the RX plane due to turbulent eddies that are approximately equal or larger than the beam diameter. Consequently, significant beam wander is expected when an optical laser beam travels from an OGSs to a satellite (uplink), with a displacement in the range of several μrad, requiring compensation techniques. Conversely, the downlink is less affected as the beam encounters the atmosphere with a considerably larger diameter compared to the sizes of turbulent eddies.

The probability distribution of the optical intensity due to beam wander is similar to that of pointing jitter and is given by [24]:

$$f(I) = \beta_w I^{\beta_w - 1} \text{with } 0 \le I \le 1 \tag{18}$$

where $\beta_w = (\hat{\theta}_d/2\sigma_{\theta,b})^2$. $\sigma_{\theta,b}$ represents the residual on-axis rms tilt error induced by the atmosphere, as explained in [42, Eq. (4.22)] [46, Eq. (10)], which accounts also for the relative motion of the satellite.

We note that all the aforementioned atmospheric beam effects are always present in any horizontal and space-ground links, even in clear sky. They cannot be avoided or solved by just increasing the transmitted power or the antenna gains, but they can be mitigated within a certain limit at system-level.

Therefore, the overall intensity fluctuations at the RX (whether on board or ground) are mainly a combination of scintillation, beam wander and residual PE. As a result, the channel fading model consists of a composite of the three associated pdfs, as detailed in the following.

G. Composite Channel Fading Model

The received irradiance at the spacecraft/OGS is determined by the composite channel resulting from the simultaneous interactions of scintillation and beam wander (in uplink), as well as pointing jitter. Therefore, the statistical properties of the received power are described by the combination of the corresponding pdfs.

The composite channel fading model, which includes the $\mathcal{GG}$ distribution (Eq. (16)) and two beta pdfs for the PE (Eq. (11)) and beam wander (Eq. (18)), is derived as follows:

$$f_{I,\mathcal{GG}}(I) = \frac{\beta_w q}{\Gamma(a)\Gamma(b)I} G_{2,4}^{4,0}\left(\frac{abI}{\bar{I}}\middle|\begin{matrix}\beta_w+1, q+1\\ q, \beta_w, a, b\end{matrix}\right) \tag{19}$$

where $G_{p,q}^{m,n}(\cdot|\cdot)$ denotes the Meijer G-function and $\bar{I}$ stands for the average value of the irradiance, with $\bar{I} = \beta_w q/(1+q)(1+\beta_w)$. The derivation steps through the Mellin transform technique and the asymptotic analysis are reported in [23]. As mentioned above, we used this pdf composition with $\mathcal{GG}$ for the link budgets in uplink. Although Eq. (19) is mathematically accurate, it suffers from computational issues in few cases; this is primarily due to numerical issues arising when values of the a and b parameters in the $\mathcal{GG}$ distribution became very large, e.g., in the weak turbulence condition or downlink.

To validate the accuracy of the novel analytic pdf, we compare it with a Monte Carlo simulation. As an example, in Fig. 7, the analytic pdf using $\mathcal{GG}$ (Eq. (19)) is depicted with a red line, representing a scenario of strong turbulence in uplink to GEO (parameters listed in Table I), assuming $\sigma_{\theta,p} = 1.3$ μrad at 30° elevation angle. The close match between the analytic pdf and the Monte Carlo results demonstrates the accuracy of the derived formulation.

The composite model for the case of $\mathcal{G}$ distribution (Eq. (17)) with PE, used in downlink, is formulated as [47].

$$f_{I,\mathcal{G}}(I) = \frac{q}{\Gamma(m)I} G_{1,2}^{2,0}\left(\frac{mqI}{(q+1)\bar{I}}\middle|\begin{matrix}1+q\\ m, 1\end{matrix}\right). \tag{20}$$

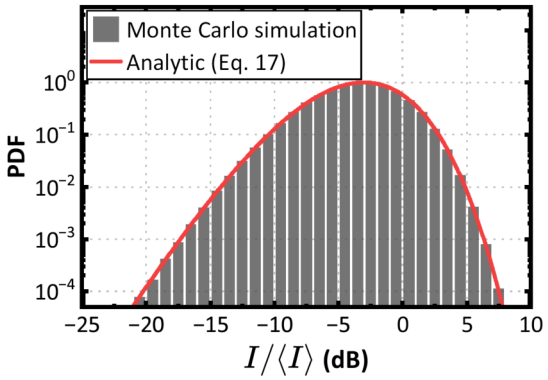

Fig. 7. Example of composite analytic channel fading model with $\mathcal{GG}$ distribution for the scintillation, beta distribution for PE and beam wander (Eq. (19)). The curve was generated for an uplink at 30° elevation angle under strong turbulence. Additionally, we present the Monte Carlo simulation (10^6 samples) to validate the accuracy of the analytic formulation.

H. Fiber Coupling

At the RX, the light collected by the telescope aperture must be coupled into a SMF [48]. While propagating, the turbulence distorts the beam wavefront, reducing the power coupled into the fiber. The coupling efficiency depends on $(D_R/r_0)^2$ [49], which indicates approximately the number of phase distortions collected by the RX telescope. In uplink, where the RX diameter is usually much smaller than r_0, only tip/tilt correction is required (no relevant phase distortion). Conversely, in downlink, when the OGS RX diameter significantly exceeds r_0, the coupling efficiency has a notable impact on the received power, as described in the following.

The fiber coupling efficiency is given by the product of the theoretical mode mismatch between the telescope pupil and the mode fiber η_{th} and a term, η_ϕ, that depends on the phase distortions at the input of the telescope. η_{th} is defined as [50]:

$$\eta_{th}(D_R, \gamma_r) = 2\frac{\left|e^{-\beta} - e^{-\beta\gamma_r}\right|^2}{\left(1-\gamma_r^2\right)\beta^2}. \tag{21}$$

In this equation, $\beta = \frac{\pi}{2}\frac{D_R\omega_0}{\lambda f}$, where f is the effective focal length of the RX telescope and ω_0 is the mode field radius of the fiber. In the ideal case, $\eta_{th} \approx 0.8$.

The term due to the phase distortions is defined as $\eta_\phi = \exp(-\sigma_\phi^2)$, where σ_ϕ^2 represents the phase variance. This parameter was extensively studied over the years [51], [52]. Without phase compensation, even assuming perfect tip/tilt correction, η_ϕ typically falls within the range of $10^{-5} - 10^{-10}$, which cannot be compensated by increasing P_T. However, in the next section, we show that this efficiency can be significantly improved by means of the AO.

III. Fading Mitigation

The joint application of various mitigation techniques is crucial to reduce deep fading events, and thus enhance the reliability and performance of FSOC systems, particularly in those scenarios affected by atmospheric turbulence and relative motion. An effective approach encompasses a robust tracking system to maintain the alignment, and a real-time AO system to improve the fiber-coupling efficiency in downlink and to potentially pre-compensate for the atmospheric aberrations in uplink.

Effective strategies include system-level techniques such as site diversity [53], involving dynamic rerouting, and spatial transmitter diversity [54], [55]. Additionally, various techniques can also be employed encompassing enhanced Forward Error Correction (FEC) or erasure codes, and the use of interleavers to spread data over time windows longer than the fades duration. This approach would mitigate deep fades by allowing FEC to operate over varying atmospheric conditions. They were presented as a possible technical solution in [56], [57], and [58]. Another technique is Automatic Repeat-reQuest (ARQ) once the system detects packet loss [59], [60], [61], [62]. However, both types of techniques result in significant latency, whilst they would also have strong requirements in terms of speed and extensive memory, which is needed to buffer the transmitted data.

In the following, we introduce the notation with $\widetilde{(\cdot)}$ to indicate the uncompensated parameters; this allows to distinguish them from the corresponding values that are obtained with fading mitigation techniques.

A. Aperture Averaging

Increasing the RX aperture diameter reduces the impact of the scintillation, since a wider telescope collects multiple turbulent patches, averaging out the irradiance fluctuations, as shown in [63] and [64]. The gain from aperture averaging scales with $(D_R/r_0)^2$, potentially resulting in a SI reduction by a factor of 100 or more. Unfortunately, the benefit of the aperture averaging is not feasible for the uplink, since the atmospheric coherence length r_0 is typically much larger (in the order of several hundreds of meters) than the satellite D_R.

B. Adaptive Optics

AO systems are commonly employed at the OGS to mitigate the atmospheric effects. The working principle involves sensing and correcting the wavefront distortions of the incoming beam to increase the received optical power. The same AO system can also be used to pre-distort the outgoing beam to mitigate the turbulence-induced effects, as demonstrated in [65]. This dual functionality enhances the reliability of optical links.

However, since the downlink and uplink paths are slightly different, the turbulence effect is not exactly the same, therefore the effectiveness of the pre-correction is strongly limited and depends on the so-called angular anisoplanatism.

The angular separation between the two paths is used to estimate the correlation of the measured wavefront from the downlink direction and the pre-distorted wavefront applied through the uplink direction. With this purpose, we introduce key angular values: Point-Ahead Angle (PAA), Iso-Planatic Angle (IPA), and Iso-Kinetic Angle (IKA), defined as in [66, Eq. (4.1)] [46, Eq. (3) and Eq. (4)]. PAA is the angular displacement of the satellite relative to the OGS, not negligible even for a GEO satellite, IPA represents the angular distance with well correlated wavefront distortions, and IKA is equivalent of IPA accounting only for low-order modes (tip and

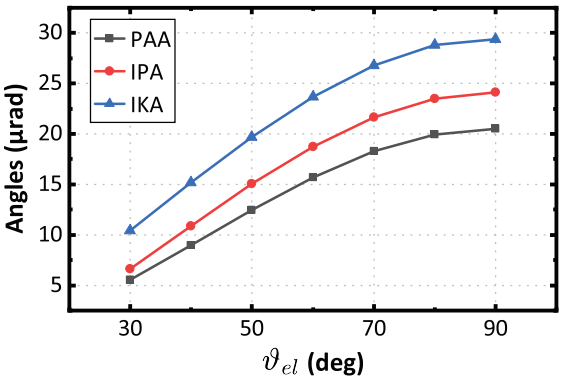

Fig. 8. Computed values of PAA, IPA and IKA for the GEO satellite under strong turbulence. The curves, generated using equations from [46, Eq. (3) and Eq. (4)], illustrate the angular correlation of wavefront distortions. Higher IPA and IKA values relative to PAA indicate better downlink and uplink correlation, aiding in effective pre-compensation.

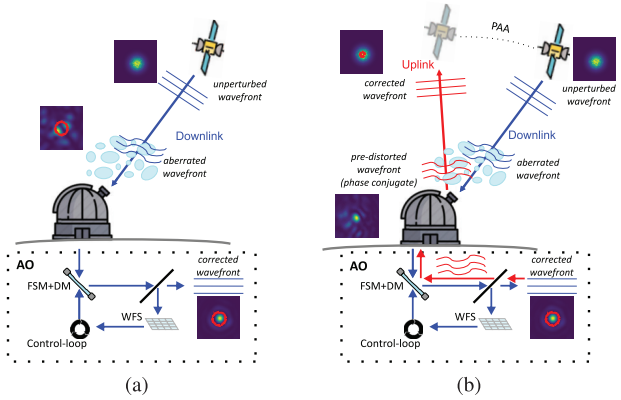

Fig. 9. Working principle of AO. In a) the downlink correction: it involves sensing a portion of the incoming beam, measuring wavefront distortions (WFS), which are sent to a control system that computes the necessary corrections and applies them to a system of mirrors. The mirrors dynamically adjust their surface to counteract the distortions, delivering (ideally) a near-diffraction-limited beam to the receiver. In b) the uplink pre-distortion: in closed-loop control, it applies corrections based on the downlink wavefront measurements to compensate for turbulence effects in the outgoing beam. AO: Adaptive Optics, WFS: WaveFront Sensor, FSM: Fast Steering Mirror, DM: Deformable Mirror.

tilt). Typical values of PAA range between $5-20$ μrad, IPA ranges between $6-24$ μrad, IKA varies approximately between $10-30$ μrad for a GEO satellite link, considering elevation angles ϑ_{el} between $30-90$ ° and strong turbulence conditions, as reported in Fig. 8. As a rule of thumb, the greater the IPA and IKA compared to PAA, the stronger the correlation between the downlink and uplink signals, resulting in more effective pre-compensation and increased received power at the satellite. In Fig. 8 we can see that the AO can be effectively pre-compensate for the low orders (beam wander) since IKA is significantly larger than PAA, but it is quite limited for the higher orders (scintillation). In the following, we will quantify the gains of the AO for both phenomena.

As depicted in Fig. 9, the main components of the AO include the Fast Steering Mirror (FSM) for tip/tilt correction, the Deformable Mirrors (DMs) for phase correction, and the WaveFront Sensor (WFS) (typically a Shack–Hartmann sensor) to measure wavefront aberrations. Operating in a

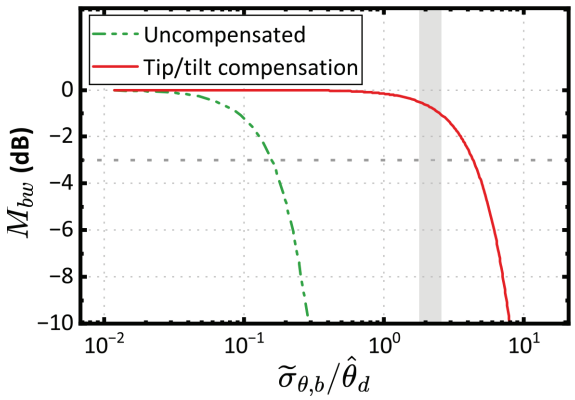

Fig. 10. M_{bw} with and without the tip/tilt compensation as a function of the uncompensated tilt error $\widetilde{\sigma}_{\theta,b}$ normalized to the divergence angle $\hat{\theta}_d$. The shaded area represents the range of $\widetilde{\sigma}_{\theta,b}/\hat{\theta}_d$ considered in this study, varying the elevation angle. Tip/tilt compensation improves the margin, reducing losses to approximately 1 dB under atmospheric condition reported in Table I. Target OP: 1×10^{-3}. The curves were generated from Eq. (22).

closed-loop configuration, this setup continuously samples and measures the downlink wavefront, providing feedback to dynamically adjust the mirrors in real-time. It can correct both low and high-order optical aberrations.

A small portion of the downlink light is directed onto the WFS, which measures the aberrations of the wavefront. The sensor data are sent into the control system for processing, which then drives the actuators to adjust the FSM and DM in real-time, correcting the wavefront distortions. This enhances fiber coupling in the downlink and applies a "corrective" or conjugate phase to the uplink beam. The FSM corrects the tilts of the wavefront in two dimensions (referred to as low-order aberrations), by means of small rotations around its two axes; this is equivalent to the correction of the position offsets in an image. The DM, on the other hand, corrects the phase distortion, enhancing fiber coupling in the downlink. The same phase-distortions are also usually applied on the uplink beam, to pre-compensate for the atmospheric effects. For effective real-time performance, the closed-loop frequency of the AO system must exceed the Greenwood frequency [67]. As strong turbulence has short coherence times (i.e., high correlation frequencies), it necessitates higher bandwidths for the WFS controllers and DM, supported by efficient algorithms, to maintain the required correction performance.

To assess the benefit of the AO on the beam wander impairment, we compute M_{bw} as a function of the uncompensated tilt error $\widetilde{\sigma}_{\theta,b}$, normalized to $\hat{\theta}_d$. Similarly to the evaluation of the maximum pointing loss, we compute M_{bw} applying Eq. (2) to the pdf of Eq. (18):

$$M_{bw} = 10\log_{10}\left(\mathrm{OP}^{\frac{1}{\beta_w}}\right) \tag{22}$$

We report the results, with and without tip/tilt pre-compensation in Fig. 10. As mentioned above, we evaluated these curves using [46, Eq. (10)]; the uncompensated curve was computed after setting the correlation functions to 0. From [46, Eqs. (11) to (13)], we can observe how the beam wander depends on the PAA and the diameter of the telescope, considered in the computation. The shaded region in Fig. 10

indicates the values of $\widetilde{\sigma}_{\theta,b}/\hat{\theta}_d$ considered in this study, varying the elevation angle. Clearly, without any compensation, the losses could be considered infinite, while applying the low-order pre-correction, we estimate around 1 dB margin. In absence of channel information from the incoming signal, i.e., without downlink or beacon signal, it is worth to note that to uphold a margin below 3 dB, $\hat{\theta}_d$ must be at least 5 times higher than $\widetilde{\sigma}_{\theta,b}$, aiming a link OP of 1×10^{-3}. This can be achieved, for instance, by decreasing D_T or by means of the beam expander, although both providing a lower received power. On the other hand, by sensing the channel through an incoming signal, $\widetilde{\sigma}_{\theta,b}$ could be reduced by pre-correcting the tip/tilt of the outgoing signal. The gain provided by this correction is appreciable in Fig. 10: to get M_{bw} below 3 dB with tip/tilt compensation, $\hat{\theta}_d$ could be as low as around one fourth of $\widetilde{\sigma}_{\theta,b}$, allowing for a higher G_T.

Finally, we evaluate the benefits derived from exploiting the full AO correction, i.e., addressing also the high-order distortions with the DM. As anticipated in Section II-H, even if tip/tilt correction is very precise, the fiber coupling efficiency remains extremely low, requiring a more effective correction of the aberrations. It was demonstrated that the phase distortion σ_ϕ could be significantly reduced by using the DMs [49], capable of correcting the high-order distortions. The effectiveness of this correction relies on the characteristics of the AO system, primarily on the number of actuators of the DM: the higher the number of actuators, the higher the number of corrected modes [68]. The residual phase variance σ_ϕ^2, for a number of the measured and corrected modes J, is given by:

$$\sigma_\phi^2 = \begin{cases} \Delta_J \left(\dfrac{D_R}{r_0}\right)^{\frac{5}{3}} & J \leq 10 \\ 0.2944\ J^{-\sqrt{3}/2} \left(\dfrac{D_R}{r_0}\right)^{\frac{5}{3}} & J > 10 \end{cases} \tag{23}$$

where Δ_J is a coefficient, which decreases with J and determines the residual errors on the phase when $J \leq 10$ modes are compensated [52]. As can be noted, the higher the J, the lower the residual phase variance, allowing for a better fiber coupling.

In Fig. 11, we report the fiber coupling efficiency $\eta_{th} \exp(-\sigma_\phi^2)$ as a function of D_R/r_0, for various J values. The gray area represents the range of D_R/r_0 investigated in this study, as outlined in Table I.

Without any beam compensation, the coupling efficiency is extremely low even for small values of D_R/r_0, corresponding to low turbulence scenarios in downlink. The efficiency slightly improves when considering tip/tilt correction ($J = 3$, in Fig. 11), but remains unacceptably low. To achieve a significant enhancement and reduce the coupling loss to an acceptable level ($|\eta_{th} \exp(-\sigma_\phi^2)| < 5$ dB), the number of corrected modes needs to increase to at least 50 ($J > 50$) considering only 90° elevation angle (i.e., $D_R/r_0 \simeq 14$). To cover the whole range of considered elevation angles, $J > 200$ is required.

It is noteworthy to highlight that η_ϕ, although primarily dependent on σ_ϕ^2, is determined by other design parameters of the AO, which further reduce the coupling efficiency. These include measurement errors, temporal errors, and residual tilt, as reported in [22] and [43].

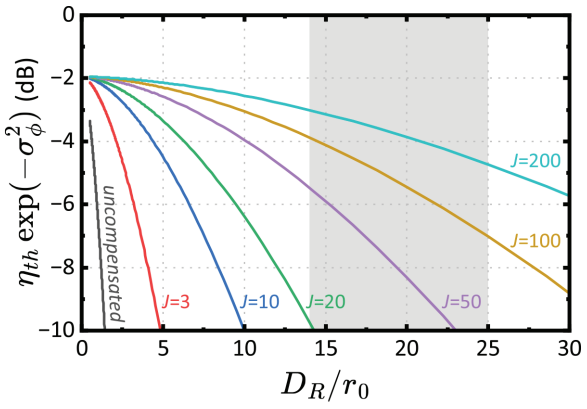

Fig. 11. Fiber coupling efficiency ($\eta_{th}\eta_\phi$) as function of D_R/r_0 for various corrected modes J {uncompensated, 3, 10, 20, 50, 100, 200}. The shaded area represents the D_R/r_0 range investigated in this work. Higher J values correspond to reduced residual phase variance, improving coupling efficiency. The curves were generated from Eqs. (21) and (23).

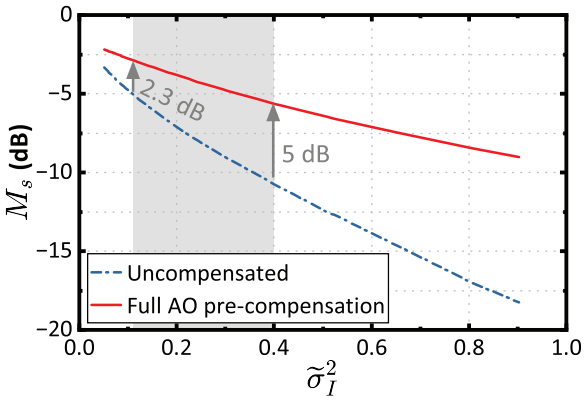

Fig. 12. M_s with and without full AO pre-distortion as function of the uncompensated SI $\widetilde{\sigma}_I^2$. The gray area illustrates the range of $\widetilde{\sigma}_I^2$ considered in this work (see Table I). Without any pre-distortion, M_s is notable, ranging approximately between 5 – 11 dB as the elevation angle decreases to 30°. Exploiting full AO, this margin decreases to 2 – 5 dB. Target OP: 1×10^{-3}.

Similarly, we assess the gain provided by the full AO correction in uplink. Referring to Fig. 9b, the WFS measurement from downlink signal – taking also into account the relative motion of the satellite – is used to calculate the required pre-distortion of the uplink wavefront. This could result in a reduction in the uplink SI [69]. To quantify the benefits, we computed M_s to consider for a target OP = 1×10^{-3} as a function of the uncompensated SI $\widetilde{\sigma}_I^2$. To determine M_s, we again exploited Eq. (2) based on the $\mathcal{GG}$ pdf reported in Eq. (16). Unlike the margins for pointing and beam wander, which can be computed analytically, we can only calculate the inverse cdf numerically. The results are shown in Fig. 12 for both uncompensated SI and with full AO correction. We first evaluated M_s over a range of SI values from 0.05 – 0.9 (dashed blue line in Fig. 12, OP = 1×10^{-3}). We repeated the evaluation of M_s, reducing the SI values by a factor of 3, as indicated in [65] and [70], where this factor was observed in a scenario comparable to that of this study (solid red line in Fig. 12, OP = 1×10^{-3}). Therefore, parameters such PAA

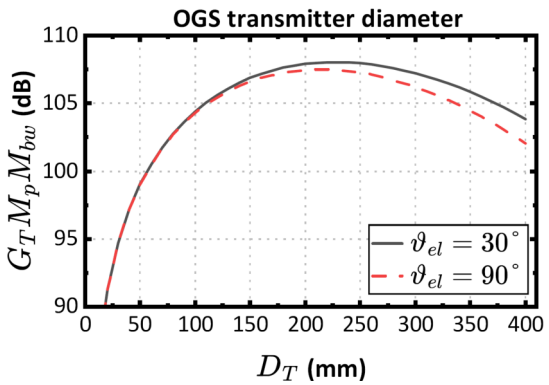

Fig. 13. Results combining the TX antenna gain and link loss (in dB) as a function of the OGS D_T for the uplink. We considered the M_p and M_{bw}, which depend on D_T, and strong turbulence, $\sigma_{\theta,p} = 1.3$ μrad, $\vartheta_{el} = \{30^\circ, 90^\circ\}$ and target OP: 1×10^{-3}. These curves were generated exploiting Eqs. (5), (12) and (22).

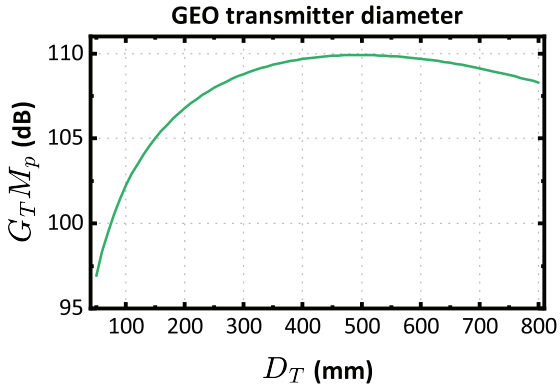

Fig. 14. Results combining the TX antenna gain and link losses (in dB) as a function of the GEO D_T for downlink scenario. We considered the M_p, which depends on D_T, and strong turbulence and target OP: 1×10^{-3}. This curve, generated by exploiting Eqs. (5) and (12), indicates the optimum GEO D_T. However, considering practical spacecraft constraints, a sub-optimal solution of 250 mm is chosen, with an acceptable performance penalty of 2 dB.

and IPA were implicitly taken from the measured data given in [65] and [70]. Both curves are reported as a function of the uncompensated SI $\widetilde{\sigma}_I^2$ to emphasize the margin gain, given a specific uncompensated SI value. The shaded region in Fig. 12 indicates the range of $\widetilde{\sigma}_I^2$ considered in this study. Without any pre-distortion, M_s is notably significant, ranging approximately between $5-11$ dB as the elevation angle decreases to 30°. Exploiting full AO, this margin decreases to $2-5$ dB. Theoretically, the reduction factor could be quite higher, but it is practically limited by anisoplanatism and residual phase distortions. We highlight that this reduction of the SI does not correspond directly to the gain in M_s, which depends on the specific pdf of the atmospheric turbulence.

IV. Telescopes Design

As mentioned, the telescope diameters play a critical role for the FSO links. At the TX, D_T determines the beam waist, thus impacting beam divergence and various related parameters, such as TX antenna gain, pointing, and beam wander losses. Conversely, at the RX, a larger diameter D_R enhances the RX antenna gain and helps reduce the beam wander by collecting multiple turbulence cells, though at the cost of fiber coupling efficiency in the downlink.

In Fig. 13, we show the product of the TX antenna gain and the losses for pointing jitter and beam wander as a function of D_T, calculated using Eqs. (5), (12) and (22). This value is calculated for two elevation angles ($\vartheta_{el} = \{30^\circ, 90^\circ\}$), in the scenario reported in Table I. The curves show a peak corresponding to the optimal D_T, which maximize the RX optical power. Referring to Fig. 13, this maximum is around $D_T = 225$ mm (200 mm) at 30° (90°) elevation angle. The two maxima are similar, therefore we selected D_T optimized for $\vartheta = 30^\circ$ elevation angle as the worst-case scenario. Note that the values in Fig. 13 do not account for the huge losses due to free-space propagation, which typically range from $250-300$ dB for Earth-to-space distances. Hence, to ensure high performance communication, it is crucial to choose telescope diameters that maximize the RX optical power.

TABLE II
Summary of the Communication and System Parameters

Parameter	Value	Condition
Optical wavelength	1550 nm	
10 Gbit/s OOK Sensitivity	25 PPB	RS(255,239)
10 Gbit/s DPSK Sensitivity	8 PPB	oFEC
100 Gbit/s DP-QPSK Sensitivity	8 PPB	oFEC
Noise figure of pre-amplifier EDFA	4 dB	
Link margin	4 dB	
OGS TX diameter	225 mm	$\gamma = 0\%$, $\eta_T = 50\%$
OGS ϑ_d	6.5 µrad	$W_0 = 10$ cm
OGS RX diameter	1000 mm	$\gamma = 30\%$, $\eta_R = 50\%$
GEO TX diameter	250 mm	$\gamma = 30\%$, $\eta_T = 50\%$
GEO ϑ_d	5.2 µrad	$W_0 = 12.2$ cm
GEO RX diameter	250 mm	$\gamma = 30\%$, $\eta_R = 50\%$
$\sigma_{\theta,p}$	1.3 µrad 1 µrad	uplink downlink
Scintillation correction factor	3	uplink [65], [73]
Number of corrected modes (J)	275	downlink

Indeed, a similar trade-off analysis was conducted for the downlink. The M_p value was calculated by considering a smooth variation in pointing jitter with telescope aperture (the larger is the telescope, the smaller is the jitter). Specifically, we assumed a value of 20 μrad for a telescope diameter of 50 mm and 0.5 μrad for a diameter of 500 mm. The curve presented in Fig. 14 shows that the optimal GEO telescope requires an aperture of 500 mm. However, practical considerations for onboard telescopes, such as size, weight, power consumption, and available space, limit feasible aperture sizes. Thus, we selected a sub-optimal aperture of 250 mm, accepting a minor 2 dB performance penalty compared to the ideal solution.

V. Optical Modulation/Detection Scheme

We selected three modulation formats with their own advantages and drawbacks, whose sensitivities – expressed in photons-per-bit (PPB) to maintain consistency in comparison – are summarized in Table II. In all configurations, the system includes FEC to correct the errors as long as pre-FEC Bit Error Ratio (BER) is lower than a given threshold. We also assumed that the RX includes a

low-noise EDFA as pre-amplifier (as shown in Fig. 2); thus, for each WDM channel, the pre-FEC BER is determined by the Optical Signal to Noise Ratio (OSNR) at the EDFA pre-amplifier output; noteworthy, as the amplifier operates in small-signal regime, the OSNR is simply fixed by the power of the channel at the EDFA input P_{in}, and by the amplifier noise figure [71]. Therefore, from the pre-FEC BER threshold (e.g., 1×10^{-2}) and the noise figure, we derive the sensitivity at the EDFA input, i.e., the P_{in} corresponding to the BER threshold. Given the bit rate, the PPB values can be easily determined. Noteworthy, the PPB values refer to the target pre-FEC BER, and are also determined by the specific modulation format, the symbol rate and the noise figure. We also note that those are the optimized values, whilst the exact values in practical cases depend (weakly) on various parameters, such as the bandwidth of the electrical and optical filters, as well as the real noise figure of the EDFA.

On the other hand, the OP is the probability that the system is out of service, which happens when the pre-FEC BER exceeds the threshold. In other words, this is the probability that P_{in} is lower than the sensitivity; as explained above, the computation of OP involves the detailed calculation of received power, including the stochastic process of high complexity.

Among the modulation formats, the simplest is the optical non-return-to-zero (NRZ)-OOK based on intensity modulation, already considered in commercial FSOC systems. The detection is based on a high-bandwidth Photo-Diode (PD). Considering a realistic 4 dB noise figure for the pre-amplifier EDFA, NRZ-OOK requires 25 PPB, when employing Reed-Solomon (RS) FEC with BER threshold of 5×10^{-3} [72], which is the standard in commercial transceivers.

A valid alternative modulation format for satellite communication, proposed also by JAXA and ONERA [7], [73], is NRZ-DPSK. This does not require coherent detection, as it can be conveniently detected using a Mach-Zehnder Delay Interferometer (MZDI) device and balanced detectors. It offers 3 dB OSNR advantage over NRZ-OOK, halving the required PPB to 12.5 [74]. However, DPSK transceivers are not widely available and an ad-hoc solution needs to be developed. If combined with an efficient FEC scheme (e.g., oFEC, which has a BER threshold at 2×10^{-2} [75]), the sensitivity can be further improved by an additional 2 dB, reducing it to 8 PPB.

Lastly, we considered DP-QPSK coherent transceivers that enable a significant increase in spectral efficiency and data rates (100 Gbit/s with a single module), thanks to coherent detection and a dedicated DSP. This has a sensitivity of 8 PPB [76] considering the oFEC, largely adopted in commercial modules. Unfortunately, despite their advantages, off-the-shelf coherent transceivers suffer from slow recovery from deep fading events [77]. Therefore, in such cases, a suitable and optimized DSP must be designed and implemented to counteract these fading events; otherwise, simpler formats might be preferred.

Currently, all the transceivers for coherent transmission in fiber integrate an ASIC for coding/decoding, DSP and FEC. It is an open issue if, on long-term, these transceivers could be modified with an ASIC optimized for FSO in space, which could have a lighter DSP and have faster recovery times, but still requires a great effort in terms of cost and human effort. We assumed the use of existing hardware, as optimized for fiber communications.

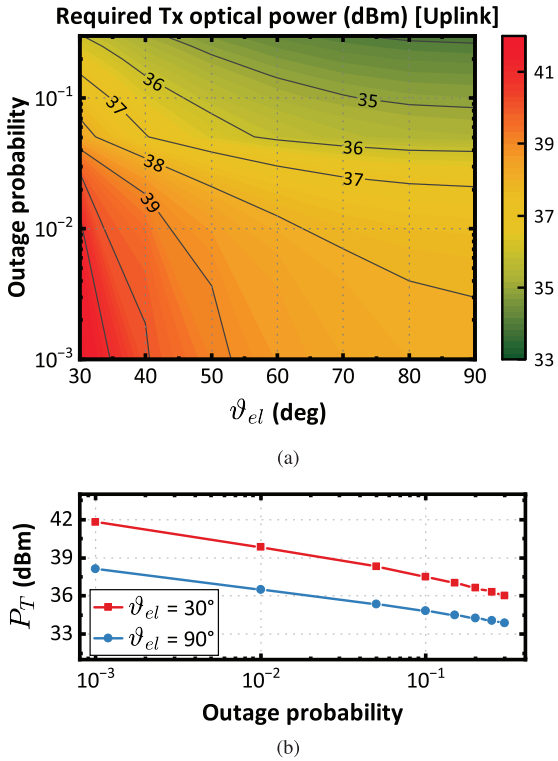

Fig. 15. (a) Required P_T as a function of the elevation angle ϑ_{el} and target OP. We considered uplink under strong turbulence with one 10 Gbit/s OOK channel. (b) Detail of the required P_T as a function of the OP at 30° and 90°.

We highlight that we considered OOK and DP-QPSK solutions designed for fiber optics and available in the market, which already include the FEC (RS for OOK and oFEC for DP-QPSK). Additionally, we view DPSK as a valid alternative thanks to its advantages in sensitivity compared to OOK. However, this last solution is not widely available, requiring the development of a custom transceiver. Therefore, we envision a DPSK transceiver with modern and more efficient FEC, such as the oFEC. If OOK-based transceivers also adopt oFEC coding, we foresee a gain of approximately 2 dB.

VI. Communication Results

We performed the optimization design study of an Earth-GEO FL, focusing on both uplink and downlink transmission requirements under different specifications. The key input parameters for the link budgets computation are conveniently summarized in Table II. As stated in Section II-B, we combined into a single composite pdf that address the statistical impacts of pointing, scintillation and beam wander, expressed by M_{pdf}. The analytical closed-form expression has been detailed in Section II-G.

In Figs. 15 and 16, we report the required P_T for both uplink and downlink transmissions. These results are shown as a function of ϑ_{el} (from 30° to 90°) considering various targets

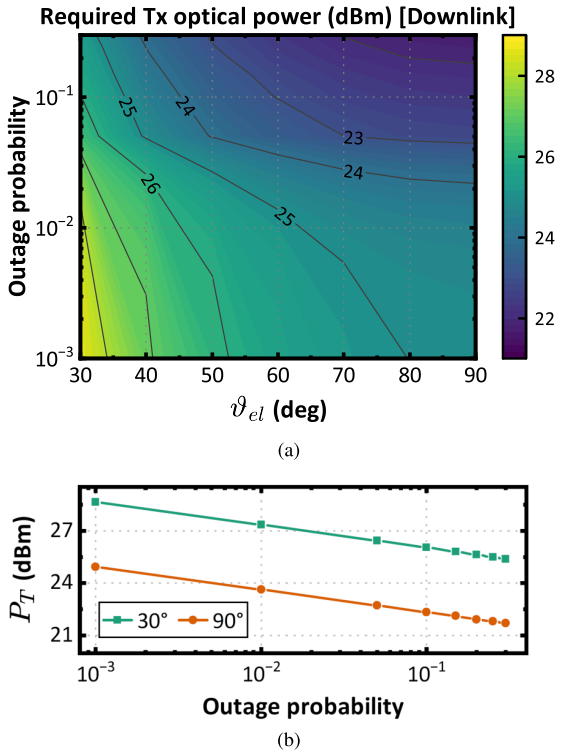

(a)

(b)

Fig. 16. (a) Required P_T as a function of the elevation angle ϑ_{el} and target OP. We considered downlink under strong turbulence with one OOK 10 Gbit/s channel. (b) Detail of the required P_T as a function of the OP at 30° and 90°.

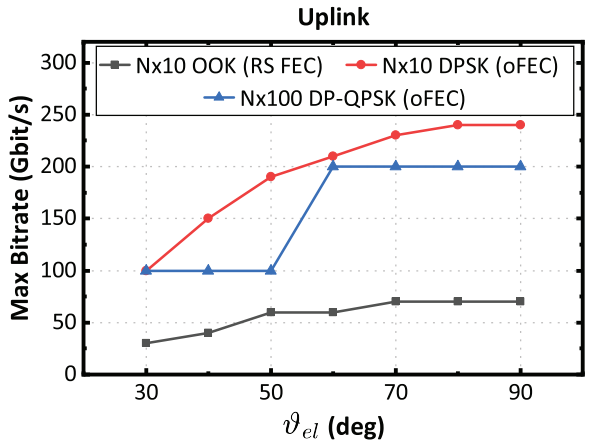

Fig. 17. Maximum achievable throughput for uplink under strong turbulence. We considered a maximum P_T = 47 dBm [78] and three different modulation schemes: $N\times10$ Gbit/s OOK, $N\times10$ Gbit/s DPSK, $N\times100$ Gbit/s DP-QPSK. Target OP: 1×10^{-3}.

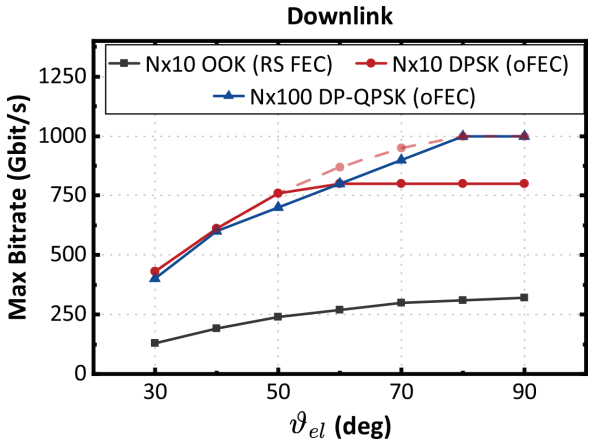

Fig. 18. Maximum achievable throughput for downlink under strong turbulence. We considered a maximum P_T = 40 dBm and three different modulation schemes: $N\times10$ Gbit/s OOK, $N\times10$ Gbit/s DPSK, $N\times100$ Gbit/s DP-QPSK. Target OP: 1×10^{-3}. The dashed red line indicates the DPSK aggregate bit rate if the number of amplified channel is not limited.

OP (from 0.3 to 1×10^{-3}). For the sake of simplicity, the data are generated for a single WDM channel (i.e., $N_{ch}=1$) at 10 Gbit/s OOK. It is then quite simple to rescale the curves for higher N_{ch} values and for the other modulation schemes, considering the different PPB reported in Table II. For instance, reducing P_T by approximately 5 dB allows the estimation for one DPSK channel at 10 Gbit/s, whilst increasing it by 5 dB accounts for one DP-QPSK channel at 100 Gbit/s. Thus, considering the PPB sensitivity values, increasing by 10 dB the computed P_T values enables the transmission of either 10 OOK channels, 30 DPSK channels, or 3 DP-QPSK channels.

Fig. 15a shows that establishing a 1×10 Gbit/s OOK uplink to GEO requires P_T = 42 dBm, achievable with commercially available boosters, assuming an OP of 1×10^{-3} and targeting $\vartheta_{el}=30°$, i.e., the worst case condition. Increasing the target OP, or increasing the elevation angle, reduces the required P_T, as expected. In particular, from Fig. 15b, we observe the difference in P_T between 30° and 90°, which is around 2 dB. We also see that P_T decreases with the target OP, as expected. For instance, relaxing the target OP from 1×10^{-3} to 1×10^{-2} allows for nearly 2 dB lower optical power.

Similarly, in Fig. 16, we report the P_T to set up the downlink, from GEO to the OGS. As can be seen, the values are considerably lower compared to the uplink scenario. This discrepancy is primarily due to the asymmetry of the channel in the two directions and the substantial difference in the D_R, which enhance G_R and significantly mitigates the effect of the scintillation. In Fig. 16b, we note that the P_T spread between 30° and 90° is slightly higher (4 dB) than the previous case, whilst the difference from 1×10^{-3} to 1×10^{-2} OP remains consistent to 2 dB.

Lastly, in Fig. 17, we present the maximum aggregated data rates for the uplink, assuming a target OP of 1×10^{-3} and P_T = 47 dBm at OGS [78]. We considered the three different modulation formats and bit rates: OOK, DPSK and DP-QPSK with 10 Gbit/s, 10 Gbit/s and 100 Gbit/s per channel, respectively. We allocated a maximum of 80 channels, each spaced by 50 GHz, within the optical C-band, which is a standard for optical fiber. While OOK and DPSK curves exhibit a smooth increase of the bit rate with ϑ_{el}, as expected, DP-QPSK shows a step-like behavior due to its granularity: from $\vartheta_{el}=30°$ to 50°, a single channel is sustainable, while above 50°, two channels can be activated, reaching an aggregate capacity of 200 Gbit/s. As a result, the most performing option is the 10 Gbit/s DPSK, which share the same PPB as 100 Gbit/s DP-QPSK, but offers better granularity.

Similar analysis was conducted also for the downlink; in this case, the maximum P_T from the space-qualified booster is set

to 40 dBm. Fig. 18 reports different results compared to uplink, thanks to the wider link margin available (see Fig. 16). DPSK and DP-QPSK exhibit nearly identical results until $\vartheta_{el} = 60°$, thus DPSK saturates the available WDM channels, reaching the maximum throughput at 800 Gbit/s ($N_{ch} = 80$), while DP-QPSK can achieve 1 Tbit/s ($N_{ch} = 10$). For completeness, we also include the DPSK aggregate bit rate in case no wavelength limitation is present (red dashed line in Fig. 18). We note that a WDM system with $N_{ch} = 80$ in a GEO terminal could represent a challenge in the design of the satellite because of space limitations; yet, this is not impossible. Noteworthy, photonic integrated circuits (PICs) with a high number of channels (>50) are already commercially available for FOC; today, there are various proposals about the use of PICs in space to minimize costs, power consumption, and size, while accommodating a high number of channels [79], [80].

VII. Conclusion

Future satellite communications will increasingly rely on WDM-FSO links to provide very high-speed connectivity among different satellites and between satellites and OGSs. These links can leverage upon devices and technologies developed for FOC and are expected to provide link speeds of hundreds of Gbit/s [3], [28]. As we explained, we expect that the first FSO systems will largely exploit the transceiver hardware from optical fiber communications: they have been largely optimized in the past, so that they are compact and already include all the electronics.

In order to achieve very high speed links, we identified the challenges at system level to establish a reliable FL with GEO satellite and then performed a detailed analysis of the individual contributions. We indicated the telescope diameter as one of the key elements, as it affects the beam divergence, enabling the mitigation of pointing and beam wander, and provided the antenna gains. In addition, the OGS RX diameter influences various mitigation techniques dependent on D_R/r_0 (e.g., fiber coupling, aperture averaging). We highlighted some required characteristics of the AO to reduce the impact of wavefront distortions. Finally, we carried out link analyses to estimate the minimum P_T for establishing a reliable communication under various conditions. Based on this analysis, we estimated the maximum achievable throughput, considering three different modulation formats and a target OP of 1×10^{-3}. The reported analyses and results demonstrate the feasibility of the links in the near future, provided that the technology can adequately support them, with state-of-the-art solutions such as High Power Optical Amplifiers (HPOAs), performing AO and sizable telescope diameters. Bit rates exceeding 100 Gbit/s are expected in Earth to GEO uplink, whereas reaching up to 1 Tbit/s in downlink, thanks to the favorable channel and system characteristics, compared to uplink. However, relevant innovations are still needed to enhance the reliability in multiple atmospheric conditions, improve the link budget, and reduce the size, weight, power and cost. Future research directions could include the development of more precise coarse pointing mechanism for larger telescope apertures compatible with terabit-per-second data rates (e.g., 250 mm Laser Communication Terminal), and new technologies for WFS as the Shack-Hartmann sensor showed limitations under severe atmospheric turbulence. In addition, to increase link availability, space diversity techniques should be considered, because optical gateways frequently suffer from link degradation and outages caused by clouds, turbulence, and aerosols. Forecasting such events will enable dynamic rerouting of data traffic to alternative OGS locations within the network. Future research could leverage upon Artificial Intelligence to optimize OGS placement across Europe. Furthermore, advancements in HPOA designs involving also countermeasures to mitigate the Non-Linear effects [81], improved interfaces between free-space and optical fibers, and the space-qualification of existing components are critical areas for further investigations.

Acknowledgment

The authors acknowledge Michalis P. Ninos for his work on models derivation. Opinions, interpretations, recommendations, and conclusions presented in this article are those of the authors and are not necessarily endorsed by ESA.

References

[1] H. Hauschildt et al., "HydRON: High throughput optical network," *Proc. SPIE*, vol. 11272, Mar. 2020, Art. no. 112720.
[2] H. Hemmati, *Deep Space Optical Communications*. Hoboken, NJ, USA: Wiley, 2006.
[3] Eur. Space Agency Std., Rev. 2.2. *ESA Specification for Terabit/sec Optical Links (ESTOL)*. Accessed: Mar. 5, 2025. [Online]. Available: https://connectivity.esa.int/sites/default/files/2024-09/ESTOL_air_interface_v2.2.pdf
[4] B. S. Robinson et al., "TeraByte InfraRed Delivery (TBIRD): A demonstration of large-volume direct-to-Earth data transfer from low- Earth orbit," *Proc. SPIE*, vol. 10524, Feb. 2018, Art. no. 105240.
[5] T. R. Brashears, "Achieving ≥ 99% link uptime on a fleet of 100G space laser inter-satellite links in LEO," *Proc. SPIE*, vol. 12877, Mar. 2024, Art. no. 1287702, doi: 10.1117/12.3005057.
[6] Mara Johnson-Groh, Qz.com. (2023). *Amazons Project Kuiper Satellites Are a Step Closer to Competing With Elon Musk's Starlink*. Accessed: Mar. 1, 2024. [Online]. Available: https://qz.com/amazonkuiper-satellites-space-laser-test-starlink-1851098098
[7] Y. Satoh, Y. Miyamoto, Y. Takano, S. Yamakawa, and H. Kohata, "Current status of Japanese optical data relay system (JDRS)," in *Proc. IEEE Int. Conf. Space Opt. Syst. Appl. (ICSOS)*, Nov. 2017, pp. 240–242.
[8] D. L. Fried, "Greenwood frequency measurements," *J. Opt. Soc. Amer. A, Opt. Image Sci.*, vol. 7, no. 5, p. 946, May 1990.
[9] L. Blarre, A. Aresta, D. Parrain, S. Poulenard, and J.-C. Richard, "Airbus defence and space high speed cross atmospheric optical comms program," in *Proc. IEEE Int. Conf. Space Opt. Syst. Appl. (ICSOS)*, Oct. 2023, pp. 19–25.
[10] G. Artaud et al., "FrOGS: French optical ground station for space laser applications," in *Proc. IEEE Int. Conf. Space Opt. Syst. Appl. (ICSOS)*. New York, NY, USA: French, Oct. 2023, pp. 182–188.
[11] C. Fuchs, F. Moll, J. Poliak, A. Reeves, and C. Schmidt, "Optical satellite links at DLR," *Proc. SPIE*, vol. 12413, Mar. 2023, Art. no. 1241306, doi: 10.1117/12.2659377.
[12] C. Fuchs et al., "Update on DLR's OSIRIS program and first results of OSIRISv1 on flying laptop," *Proc. SPIE*, vol. 10910, pp. 171–180, Mar. 2019.
[13] J. Poliak, R. M. Calvo, and F. Rein, "Demonstration of 1.72 Tbit/s optical data transmission under worst-case turbulence conditions for ground-to-geostationary satellite communications," *IEEE Commun. Lett.*, vol. 22, no. 9, pp. 1818–1821, Sep. 2018.
[14] A. Dochhan, J. Poliak, J. Surof, M. Richerzhagen, H. F. Kelemu, and R. M. Calvo, "13.16 Tbit/s free-space optical transmission over 10.45 km for geostationary satellite feeder-links," in *Proc. Photonic Netw., 20th ITG-Symp.*, May 2019, pp. 1–3.
[15] E. Ciaramella, V. Spirito, and G. Cossu, "Designing high-speed GEOto-Moon optical wireless communication links," *J. Opt. Commun. Netw.*, vol. 16, no. 1, p. 21, 2024.

[16] H. Kotake et al., "Experimental analysis of atmospheric channel model with misalignment fading for GEO satellite-to-ground optical link using LUCAS; onboard optical data relay satellite," *Opt. Exp.*, vol. 31, no. 13, pp. 21351–21366, Jun. 2023. [Online]. Available: https://opg.optica.org/oe/abstract.cfm?URI=oe-31-13-21351

[17] S. M. Walsh et al., "Demonstration of 100 Gbps coherent free-space optical communications at LEO tracking rates," *Sci. Rep.*, vol. 12, no. 1, p. 18345, Oct. 2022.

[18] B. J. Klein and J. J. Degnan, "Optical antenna gain. 1: Transmitting antennas," *Appl. Opt.*, vol. 13, no. 9, pp. 2134–2141, Sep. 1974.

[19] E. M. Drège, N. G. Skinner, and D. M. Byrne, "Analytical far-field divergence angle of a truncated Gaussian beam," *Appl. Opt.*, vol. 39, no. 27, pp. 4918–4925, Sep. 2000.

[20] R. K. Tyson, "Adaptive optics and ground-to-space laser communications," *Appl. Opt.*, vol. 35, no. 19, p. 3640, Jul. 1996. [Online]. Available: https://opg.optica.org/ao/abstract.cfm?URI=ao-35-19-3640

[21] R. Tyson, *Introduction to Adaptive Optics* (Online Access With Subscription: SPIE Digital Library). Bellingham, WA, USA: Society of Photo Optical, 2000. https://books.google.it/books?id=qbMZOkkNmuEC

[22] R. Tyson and B. Frazier, *Field Guide to Adaptive Optics* (Field Guides). Bellingham, WA, USA: SPIE Press, 2012.

[23] M. P. Ninos, V. Spirito, G. Cossu, and E. Ciaramella, "Outage performance of uplink pre-amplified FSO links over turbulence, beam wander, and pointing errors," *IEEE Commun. Lett.*, vol. 27, no. 12, pp. 3275–3279, Dec. 2023.

[24] R. Barrios, "Fading loss for Earth-to-space lasercom affected by scintillation and beam wander composite channel," *Opt. Eng.*, vol. 59, no. 5, 2020, Art. no. 056103.

[25] C. Cantore, D. Monopoli, A. Altamura, A. Mengali, M. Grande, and A. D'Orazio, "Link budget analysis of bi-directional LEO and GEO optical feeder links advancing the beam wander model's accuracy," *Sci. Rep.*, vol. 14, no. 1, p. 8579, Apr. 2024, doi: 10.1038/s41598-024-59198-x.

[26] D. Giggenbach, M. T. Knopp, and C. Fuchs, "Link budget calculation in optical LEO satellite downlinks with on/off-keying and large signal divergence: A simplified methodology," *Int. J. Satell. Commun. Netw.*, vol. 41, no. 5, pp. 460–476, Sep. 2023, doi: 10.1002/sat.1478.

[27] M. Toyoshima, T. Jono, K. Nakagawa, and A. Yamamoto, "Optimum divergence angle of a Gaussian beam wave in the presence of random jitter in free-space laser communication systems," *J. Opt. Soc. Amer. A, Opt. Image Sci.*, vol. 19, no. 3, pp. 567–571, Mar. 2002.

[28] E. Ciaramella et al., "1.28 terabit/s (32×40 Gbit/s) WDM transmission system for free space optical communications," *IEEE J. Sel. Areas Commun.*, vol. 27, no. 9, pp. 1639–1645, Dec. 2009.

[29] H. Uetsuka, "AWG technologies for dense WDM applications," *IEEE J. Sel. Topics Quantum Electron.*, vol. 10, no. 2, pp. 393–402, Mar. 2004.

[30] G. Cossu, V. Spirito, M. P. Ninos, and E. Ciaramella, "Design challenges in high-throughput WDM-FSO systems for satellite communications," in *Proc. 23rd Int. Conf. Transparent Opt. Netw. (ICTON)*, Jul. 2023, pp. 1–4.

[31] A. Carrasco-Casado and R. Mata-Calvo, *Space Optical Links for Communication Networks*. Cham, Switzerland: Springer, 2020, pp. 1057–1103.

[32] F. Duarte, *Tunable Laser Optics*. New York, NY, USA: Taylor & Francis, 2015.

[33] J. Kauffman, "The calculated radiation patterns of a truncated Gaussian aperture distribution," *IEEE Trans. Antennas Propag.*, vol. AP-13, no. 3, pp. 473–474, May 1965.

[34] A. L. Buck, "The radiation pattern of a truncated Gaussian aperture distribution," *Proc. IEEE*, vol. 55, no. 3, pp. 448–450, Mar. 1967.

[35] R. Barrios, S. Dimitrov, R. Mata-Calvo, and D. Giggenbach, "Link budget assessment for GEO feeder links based on optical technology," *Int. J. Satell. Commun. Netw.*, vol. 39, no. 2, pp. 160–177, Mar. 2021.

[36] J. J. Degnan and B. J. Klein, "Optical antenna gain. 2: Receiving antennas," *Appl. Opt.*, vol. 13, no. 10, pp. 2397–2401, Oct. 1974.

[37] D. Vasylyev, W. Vogel, and F. Moll, "Satellite-mediated quantum atmospheric links," *Phys. Rev. A, Gen. Phys.*, vol. 99, no. 5, May 2019, Art. no. 053830.

[38] H. Weichel, *Laser Beam Propagation in the Atmosphere*, vol. 10319. Bellingham, WA, USA: SPIE Press, 1990.

[39] A. Prokes, O. Wilfert, and J. Petrzela, "Comparison of atmospheric losses in 850 nm and 1550 nm optical windows," in *Proc. IEEE Region 8 Int. Conf. Comput. Technol. Electr. Electron. Eng. (SIBIRCON)*, Jul. 2010, pp. 310–313.

[40] I. I. Kim, B. McArthur, and E. J. Korevaar, "Comparison of laser beam propagation at 785 nm and 1550 nm in fog and haze for optical wireless communications," in *Optical Wireless Communications III*, vol. 4214, E. J. Korevaar, Ed., Bellingham, WA, USA: SPIE, 2001, pp. 26–37, doi: 10.1117/12.417512.

[41] L. C. Andrews and R. L. Phillips, *Laser Beam Propagation Through Random Media*. Bellingham, WA, USA: SPIE, 2005.

[42] R. J. Sasiela, *Electromagnetic Wave Propagation in Turbulence: Evaluation and Application of Mellin Transforms*, vol. 18. Cham, Switzerland: Springer, 2012.

[43] J. W. Hardy, *Adaptive Optics for Astronomical Telescopes*. Oxford, U.K.: Oxford Univ. Press, Jul. 1998, p. 448.

[44] M. Beason, S. Gladysz, and L. Andrews, "Comparison of probability density functions for aperture-averaged irradiance fluctuations of a Gaussian beam with beam wander," *Appl. Opt.*, vol. 59, no. 20, p. 6102, Jul. 2020. [Online]. Available: https://opg.optica.org/ao/abstract.cfm?URI=ao-59-20-6102

[45] L. C. Andrews, R. L. Phillips, R. J. Sasiela, and R. Parenti, "PDF models for uplink to space in the presence of beam wander," *Proc. SPIE*, vol. 6551, May 2007, Art. no. 655109.

[46] D. Alaluf and J. M. P. Armengol, "Ground-to-satellite optical links: How effective is an uplink tip/tilt pre-compensation based on the satellite signal?," *CEAS Space J.*, vol. 14, no. 2, pp. 227–238, Apr. 2022.

[47] H. Sandalidis, "Performance analysis of a laser ground-station-to-satellite link with modulated gamma-distributed irradiance fluctuations," *J. Opt. Commun. Netw.*, vol. 2, no. 11, pp. 938–943, Nov. 2010.

[48] M. Toyoshima, "Maximum fiber coupling efficiency and optimum beam size in the presence of random angular jitter for free-space laser systems and their applications," *J. Opt. Soc. Amer. A, Opt. Image Sci.*, vol. 23, no. 9, pp. 2246–2250, Sep. 2006.

[49] M. Chen, C. Liu, and H. Xian, "Experimental demonstration of singlemode fiber coupling over relatively strong turbulence with adaptive optics," *Appl. Opt.*, vol. 54, no. 29, p. 8722, Oct. 2015.

[50] M. T. Gruneisen, M. B. Flanagan, and B. A. Sickmiller, "Modeling satellite-Earth quantum channel downlinks with adaptive-optics coupling to single-mode fibers," *Opt. Eng.*, vol. 56, no. 12, p. 126111, 2017.

[51] D. L. Fried, "Statistics of a geometric representation of wavefront distortion," *J. Opt. Soc. Amer.*, vol. 55, no. 11, p. 1427, Nov. 1965.

[52] R. J. Noll, "Zernike polynomials and atmospheric turbulence," *J. Opt. Soc. Amer.*, vol. 66, no. 3, pp. 207–211, 1976.

[53] E. Erdogan, I. Altunbas, G. K. Kurt, M. Bellemare, G. Lamontagne, and H. Yanikomeroglu, "Site diversity in downlink optical satellite networks through ground station selection," *IEEE Access*, vol. 9, pp. 31179–31190, 2021.

[54] T. A. Tsiftsis, H. G. Sandalidis, G. K. Karagiannidis, and M. Uysal, "FSO links with spatial diversity over strong atmospheric turbulence channels," in *Proc. IEEE Int. Conf. Commun.*, Beijing, China, Dec. 2008, pp. 5379–5384.

[55] I. I. Kim, H. Hakakha, P. Adhikari, E. J. Korevaar, and A. K. Majumdar, "Scintillation reduction using multiple transmitters," *Proc. SPIE*, vol. 2990, pp. 102–113, Apr. 1997, doi: 10.1117/12.273685.

[56] D. R. Arrieta et al., "Block interleaver dimensioning and real-time demonstration for Ground-to-Satellite optical communications," in *Proc. Eur. Conf. Opt. Commun. (ECOC)*, Sep. 2022, pp. 1–4.

[57] D. Zhang, S. Hao, Q. Zhao, L. Wang, Q. Zhao, and X. Wan, "Highthroughput interleaving scheme in free space optical communication system," in *Proc. IEEE 17th Int. Conf. Commun. Technol. (ICCT)*, Oct. 2017, pp. 640–644.

[58] J. A. Greco, "Design of the high-speed framing, FEC, and interleaving hardware used in a 5.4km free-space optical communication experiment," *Proc. SPIE*, vol. 7464, Aug. 2009, Art. no. 746409, doi: 10.1117/12.826309.

[59] G. D. Chondrogiannis, N. A. Mitsiou, N. D. Chatzidiamantis, A.-A. A. Boulogeorgos, and G. K. Karagiannidis, "Power-optimal HARQ protocol for reliable free space optical communication," in *Proc. IEEE Int. Conf. Commun. Workshops (ICC Workshops)*, May 2023, pp. 1765–1770.

[60] C. M. Schieler et al., "Recent on-orbit results and ARQ performance analysis for the TBIRD 200-gbps mission," in *Proc. IEEE Int. Conf. Space Opt. Syst. Appl. (ICSOS)*, Oct. 2023, pp. 49–55.

[61] V. V. Mai, T. C. Thang, and A. T. Pham, "Performance analysis of TCP over free-space optical links with ARQ-SR," in *Proc. 18th Eur. Conf. Netw. Opt. Commun. 8th Conf. Opt. Cabling Infrastruct. (NoC-OC&I)*, Jul. 2013, pp. 105–112.

[62] V. V. Mai and A. T. Pham, "Cross-layer designs and analysis of adaptiverate transmission and ARQ for free-space optical communications," *IEEE Photon. J.*, vol. 8, no. 1, pp. 1–15, Feb. 2016.

[63] H. T. Yura and R. F. Lutomirski, *Aperture Averaging of Optical Scintillation*. Santa Monica, CA, USA: RAND Corporation, 1969.
[64] V. Spirito, G. Cossu, and E. Ciaramella, "Feasibility study of a Terabit/s GEO-to-ground WDM optical communication link," *Proc. SPIE*, vol. 12777, Jul. 2023, Art. no. 127776.
[65] I. R. Hristovski, "Pre-distortion adaptive optics: Experimental results from bi-directional tracking links between DLRs optical ground station and Alphasats TDP-1 terminal," *Proc. SPIE*, vol. 12877, Mar. 2024, Art. no. 1287718.
[66] H. Kaushal, V. K. Jain, and S. Kar, *Acquisition, Tracking, and Pointing*. New Delhi, India: Springer, 2017, pp. 119–137. [Online]. Available: 10.1007/978-81-322-3691-74.
[67] D. P. Greenwood, "Bandwidth specification for adaptive optics systems," *J. Org. Soc. Amer.*, vol. 67, no. 3, pp. 390–393, Mar. 1977. [Online]. Available: https://opg.optica.org/abstract.cfm?URI=josa-67-3-390
[68] M. Carbillet, É. Aristidi, C. Giordano, and J. Vernin, "Anisoplanatic error evaluation and wide-field adaptive optics performance at dome C, Antarctica," *Monthly Notices Roy. Astronomical Soc.*, vol. 471, no. 3, pp. 3043–3050, Nov. 2017.
[69] J. Osborn, M. J. Townson, O. J. D. Farley, A. Reeves, and R. M. Calvo, "Adaptive optics pre-compensated laser uplink to LEO and GEO," *Opt. Exp.*, vol. 29, no. 4, pp. 6113–6132, Feb. 2021.
[70] J.-M. Conan et al., "Adaptive optics for GEO-feeder links: From performance analysis via reciprocity based models to experimental demonstration," in *Proc. Commun. Observ. Through Atmos. Turbulence, Characterization Mitigation (COAT)-Workshop*. Châtillon, France: ONERA, Dec. 2019, pp. 1–10. Accessed: Mar. 2025, doi: 10.34693/COAT2019-S5-003. [Online]. Available: https://hal.science/hal-03206080
[71] G. Agrawal, *Fiber-Optic Communication Systems*. Hoboken, NJ, USA: Wiley, 2021.
[72] *Forward Error Correction for High Bit-Rate DWDM Submarine Systems*, document ITU, ITU-T G. 975.1 Recommendation, Series G Recommendation: Transmission Systems and Media, Digital Systems and Networks: Digital Sections and Digital Line SystemsOptical Fibre Submarine Cable Systems, 2004.
[73] P. Cyril et al., "FEELINGS: The ONERA's optical ground station for geo feeder links demonstration," in *Proc. IEEE Int. Conf. Space Opt. Syst. Appl. (ICSOS)*, Mar. 2022, pp. 255–260.
[74] P. J. Winzer and R.-J. Essiambre, "Advanced optical modulation formats," *Proc. IEEE*, vol. 94, no. 5, pp. 952–985, May 2006.
[75] OpenZR+ Multi-Source Agreement (MSA) Group, *OpenZR+ Specifications, Version 3.0*, Sep.~12, 2023. Accessed: Mar.5, 2025. [Online]. Available: https://openzrplus.org/resources/openzr-specifications-v-3-0/
[76] J. Karaki et al., "Dual-polarization multi-band OFDM versus singlecarrier DP-QPSK for 100 Gb/s long-haul WDM transmission over legacy infrastructure," *Opt. Exp.*, vol. 21, no. 14, p. 16982, Jul. 2013.
[77] G. Cossu, A. Sgambelluri, F. Paolucci, and E. Ciaramella, "How can commercial fiber equipment cope with the random fadings of FSO links?," in *Proc. Eur. Conf. Exhib. Org. Commun. (ECOC)*, Oct. 2023, pp. 1346–1349.
[78] M. Welch et al., "High power WDM sources for laser communication," *Proc. SPIE*, vol. 11993, Mar. 2022, Art. no. 119930.
[79] M. Ziarko, G. Terrasanta, N. Bergamasco, and J. Poliak, "Photonic integrated circuits for high-throughput optical communications and ranging satellite links," *Proc. SPIE*, vol. 12877, Mar. 2024, Art. no. 128770, doi: 10.1117/12.3001792.
[80] M. Baier et al., "100-channel WDM rx-type PIC on InP for use of lowcost and low power consumption electronics," in *Proc. Eur. Conf. Opt. Commun. (ECOC)*, Sep. 2014, pp. 1–3.
[81] E. Ciaramella and G. Cossu, "Nonlinear fiber effects in ultra-high power 10×10 Gbit/s WDM-IM free-space systems for satellite links," *Opt. Exp.*, vol. 32, no. 5, pp. 7959–7968, 2024. [Online]. Available: https://opg.optica.org/oe/abstract.cfm?URI=oe-32-5-7959

Veronica Spirito received the master's degree (summa cum laude) in electronics engineering from Sapienza Università di Roma and the Ph.D. degree in photonic technologies from Sant'Anna School of Advanced Studies, Pisa, Italy. Her Ph.D. research focused on channel modeling, E2E physical layer analysis for high-throughput FSOC systems, and the development of optical wireless links for extra-spacecraft communications, while her Master's thesis explored digital coherent receivers for FSOC. She is currently a Communication Systems and Technologies Engineer at European Space Agency (ESA-ESTEC, The Netherlands), specializing in design and analysis of satellite communication systems. Her expertise includes end-to-end system modeling, link budget analysis, channel impairment mitigation, and optical/ RF modulation and coding, with a focus on high data rate satellite optical networks. Throughout her career, Veronica has contributed to key ESA-led projects, such as HydRON, IRIS^2, and several ARTES activities, which brought her also to German Aerospace Center (DLR), Munich, working on adaptive optics systems and actively involved in field trials demonstrating pre-distortion adaptive optics for GEO satellites. She is also involved in standardization efforts for optical satellite communications, driving innovation in next-generation optical networks for space applications.

Ernesto Ciaramella (Senior Member, IEEE) has been a Full Professor in telecommunications with the Istituto TeCIP, Scuola Superiore Sant'Anna, Pisa, since 2014. He joined Scuola Superiore Sant'Anna as an Associate Professor in 2002. His research interests include various areas of optical communications (components, systems, and networks). His main research contributions are related to devices for the regeneration of the optical signal, design of WDM systems for transport networks and access, and free-space optical systems (optical wireless). He is the author or co-author of about 250 publications and holds 25 international patents. He participated in several European research projects. He was the Scientific Coordinator of the EU-FP7 Project COCONUT (2012–2015). He is also a Principal Investigator of ESA-TOWS Project, developing new optical wireless systems for intra-spacecraft communications.

Giulio Cossu (Member, IEEE) received the M.S. degree in physics from the University of Pisa, Italy, in 2010, and the Ph.D. degree from Scuola Superiore Sant'Anna (SA), Pisa, in 2014. Currently, he is an Assistant Professor with SA. His research is the investigation of innovative solutions for optical wireless communications (OWC), including the areas of optical propagation through the atmosphere, optical characterization, and optical communications. He was the scientific responsible for SA in the projects "High Throughput Optical Network (HYDRON)" and "HYDRON Simulation TestBed," both funded by European Space Agency (ESA). He was involved in the development of optical wireless links for intra/extra spacecraft and AIT scenarios within the framework of the TOWS project, funded by ESA. He is the author or co-author of about 100 publications and holds four international patents.

Open Access funding provided by 'CARE-CRUI 2024 Overflow' within the CRUI CARE Agreement